

ARTICLE

Chloride intracellular channel 1 cooperates with potassium channel EAG2 to promote medulloblastoma growth

Michelle A. Francisco^{1,2} , Siyi Wanggou^{1,2,3,4}, Jerry J. Fan^{1,2,5} , Weifan Dong^{1,2,5}, Xin Chen^{1,2}, Ali Momin^{1,2,5}, Namal Abeyundara^{1,2}, Hyun-Kee Min^{1,2,5}, Jade Chan^{1,2,5}, Rochelle McAdam^{1,2,5}, Marian Sia^{1,2}, Ronwell J. Pusong^{1,2} , Shixuan Liu^{5,6} , Nish Patel⁶, Vijay Ramaswamy^{1,2}, Noriyuki Kijima^{1,2}, Lu-Yang Wang^{7,8} , Yuanquan Song^{9,10} , Ran Kafri^{5,6}, Michael D. Taylor^{1,2,11,12}, Xuejun Li^{3,4} , and Xi Huang^{1,2,5} 

Ion channels represent a large class of drug targets, but their role in brain cancer is underexplored. Here, we identify that chloride intracellular channel 1 (CLIC1) is overexpressed in human central nervous system malignancies, including medulloblastoma, a common pediatric brain cancer. While global knockout does not overtly affect mouse development, genetic deletion of CLIC1 suppresses medulloblastoma growth in xenograft and genetically engineered mouse models. Mechanistically, CLIC1 enriches to the plasma membrane during mitosis and cooperates with potassium channel EAG2 at lipid rafts to regulate cell volume homeostasis. CLIC1 deficiency is associated with elevation of cell/nuclear volume ratio, uncoupling between RNA biosynthesis and cell size increase, and activation of the p38 MAPK pathway that suppresses proliferation. Concurrent knockdown of CLIC1/EAG2 and their evolutionarily conserved channels synergistically suppressed the growth of human medulloblastoma cells and *Drosophila melanogaster* brain tumors, respectively. These findings establish CLIC1 as a molecular dependency in rapidly dividing medulloblastoma cells, provide insights into the mechanism by which CLIC1 regulates tumorigenesis, and reveal that targeting CLIC1 and its functionally cooperative potassium channel is a disease-intervention strategy.

Introduction

Brain tumors are the leading cause of cancer-related deaths in children and young adults. As a high-grade brain tumor at the hindbrain, medulloblastoma (MB) is one of the most common pediatric malignant brain tumors. Conventional treatment, which includes surgery, chemotherapy, and radiation therapy, is toxic and produces lifelong side effects such as reduced IQ, growth failure, lowered physical performance, and early aging (Edelstein et al., 2011; Frange et al., 2009). MB is composed of four distinct subgroups (WNT, SHH, group 3, and group 4) and further subtypes within each subgroup, which display distinct molecular profiles and clinical features (Cavalli et al., 2017; Taylor et al., 2012). Targeted therapy, which inhibits the SHH pathway receptor Smoothed (SMO), has been developed for SHH pathway-driven MB (SHH MB). After displaying initial efficacy, tumors

acquire drug resistance, and relapse is almost always fatal (Rudin et al., 2009). These observations highlight the effectiveness of molecularly targeted therapy and the need to identify novel targets for developing combinatorial therapy. As mouse SHH MB arises from the cerebellar granule neuron precursors (CGNPs), loss of one allele of the SHH pathway inhibitor *Ptch1* in *Ptch1*^{-/-} mice results in 20% MB occurrence (Goodrich et al., 1997). *Math1-Cre; SmoM2* mice display constitutive activation of the SHH pathway in CGNPs due to expression of SmoM2 (the constitutively active mutant form of Smo), driven by the CGNP-specific driver *Math1-Cre*. As a result, *Math1-Cre; SmoM2* mice develop fully penetrant MBs (Schüller et al., 2008). Studies using the genetic mouse models of SHH MB and xenograft models of human MB can identify new disease mechanisms and therapeutic targets.

¹Program in Developmental and Stem Cell Biology, The Hospital for Sick Children, Toronto, Ontario, Canada; ²Arthur and Sonia Labatt Brain Tumour Research Centre, The Hospital for Sick Children, Toronto, Ontario, Canada; ³Department of Neurosurgery, Xiangya Hospital, Central South University, Changsha, Hunan, China; ⁴Hunan International Scientific and Technological Cooperation Base of Brain Tumor Research, Xiangya Hospital, Central South University, Changsha, Hunan, China; ⁵Department of Molecular Genetics, University of Toronto, Toronto, Ontario, Canada; ⁶Program in Cell Biology, The Hospital for Sick Children, Toronto, Ontario, Canada; ⁷Program in Neurosciences and Mental Health, The Hospital for Sick Children, Toronto, Ontario, Canada; ⁸Department of Physiology, University of Toronto, Toronto, Ontario, Canada; ⁹The Raymond G. Perelman Center for Cellular and Molecular Therapeutics, The Children's Hospital of Philadelphia, Philadelphia, PA; ¹⁰Department of Pathology and Laboratory Medicine, University of Pennsylvania, Philadelphia, PA; ¹¹Department of Surgery, University of Toronto, Toronto, Ontario, Canada; ¹²Department of Laboratory Medicine and Pathobiology, University of Toronto, Toronto, Ontario, Canada.

Correspondence to Xi Huang: xi.huang@sickkids.ca; Xuejun Li: lxjneuro@csu.edu.cn.

© 2020 Francisco et al. This article is distributed under the terms of an Attribution–Noncommercial–Share Alike–No Mirror Sites license for the first six months after the publication date (see <http://www.rupress.org/terms/>). After six months it is available under a Creative Commons License (Attribution–Noncommercial–Share Alike 4.0 International license, as described at <https://creativecommons.org/licenses/by-nc-sa/4.0/>).

Ion channels are pore-forming, transmembrane proteins that regulate biological processes by controlling ion passage across cell membranes (Hille, 2001). The opening of ion channel pores allows the flux of ions, including potassium, chloride, calcium, or sodium, based on their electrochemical gradient. Ion channels constitute a large class of drug targets for human diseases, such as neurological and cardiovascular disorders (Clare, 2010). However, ion channel function in cancer is underexplored, and its role in pediatric brain tumors was unknown before our studies. We reported that potassium channel EAG2 is up-regulated in ~15% of human MB across molecular subgroups. Genetic deletion of EAG2 suppressed MB growth in preclinical mouse models (Huang et al., 2012). We identified the US Food and Drug Administration-approved anti-psychotic drug thioridazine as an EAG2 blocker and demonstrated its anti-MB efficacy in mice. We treated a patient with SHH MB, which was resistant to the standard chemo- and radiation-therapy, using thioridazine. The positron emission tomography-computed tomography imaging revealed marked reduction of his tumor, demonstrating a response to the thioridazine therapy (Huang et al., 2015). Therefore, we identified MB dependency on over-expressed ion channels that can be therapeutically targeted.

Cell volume regulation is fundamental to many cellular behaviors, such as proliferation, apoptosis, and migration. Ionic flux across the plasma membrane serves as a mechanism to control intracellular osmolarity, the movement of nonprotein-bound water molecules, and cell volume increase or decrease. Mammalian cell volume undergoes stereotypical oscillations during cell cycle progression. Live imaging studies have shown that cells increase in volume at interphase, reduce volume before mitotic entry, and reach a minimal volume at metaphase, after which the cell volume increases during anaphase and telophase to facilitate cytokinesis (Habela and Sontheimer, 2007; Boucrot and Kirchhausen, 2008). Importantly, a recent study using budding yeast and human fibroblasts demonstrated that while cells scale up protein and RNA biosynthesis in accordance to cell growth and volume increase, excessive cell size beyond a certain level results in increased cytoplasm/DNA ratio (cytoplasm dilution). Enlarged cells undergo cell cycle arrest due to their inability to proportionally match macromolecule biosynthesis to their increased cell size (Neurohr et al., 2019). EAG2 localizes to the plasma membrane during late G2 phase and mitosis to promote potassium efflux and cell volume decrease to ensure mitotic entry and successful mitosis in MB (Huang et al., 2012). As cation and anion channels often function together to regulate cellular behaviors, we reason that a hitherto-unknown anionic channel functionally couples with EAG2 to maintain electroneutrality and coregulate MB malignancy through controlling cell volume homeostasis.

Chloride is a major anion and electrolyte that contributes to the osmotic pressure across the plasma membrane. Chloride intracellular channel 1 (CLIC1) belongs to a family of six CLICs (CLIC1-CLIC6). CLIC1 can exist as either a soluble cytosolic or a membrane protein, and the ion channel activity of CLIC1 has been shown by multiple groups (Littler et al., 2010). CLIC1 channel activity is increased by oxidation, low pH (Tulk et al., 2002; Warton et al., 2002), and cholesterol-rich lipid rafts

(Hossain et al., 2016; Valenzuela et al., 2013). CLIC1 permeates several anions (e.g., Cl^- , SCN^- , F^- , and HCO_3^-) in overexpression systems (Singh and Ashley, 2006; Valenzuela et al., 1997) and forms a chloride channel in microglia cells (Novarino et al., 2004). CLIC1 can localize to intracellular organelles such as phagosomes in macrophage and dendritic cells, where it is thought to increase phagosome chloride concentration to counterbalance the charge difference induced by proton entry (Jiang et al., 2012; Salao et al., 2016). Given its presence as a soluble protein in the cytosol, phylogenetic prediction suggests that CLIC1 may have enzymatic function (Littler et al., 2010), and soluble CLIC1 displays glutathione-dependent oxidoreductase activity in a cell-free system (Al Khamici et al., 2015). Clc1 knockout mice were viable and fertile and appeared normal, aside from showing a mild defect in platelets and macrophages (Qiu et al., 2010; Ulmasov et al., 2017).

CLIC1 overexpression has been reported in cancers of the lung, bladder, gastrointestinal tract, and glioma (Chen et al., 2007; Ding et al., 2015; Jia et al., 2016; Lu et al., 2015; Wang et al., 2011; Zhang et al., 2013). CLIC1 knockdown decreased glioblastoma (GBM) cell growth in vitro and xenograft tumor growth in mice (Setti et al., 2013). While CLIC1 knockdown inhibited cancer cell growth in most contexts, CLIC1 deficiency was reported to increase the proliferation of gastric cancer cells (Ma et al., 2012). In *Xenopus laevis*, CLIC1 in nontransformed cells exerted long-range suppression of mutant KRAS-induced tumorigenesis (Chernet and Levin, 2014). Therefore, different studies have implicated CLIC1 as either an oncogene or a tumor suppressor, but no direct mechanism for either role has been reported. Given what is known about CLIC1 in cancer, there are multiple knowledge gaps. First, how widespread is CLIC1 overexpression in human central nervous system (CNS) malignancies? Second, what is the in vivo role of CLIC1 in tumor initiation and progression (which cannot be fully addressed by in vitro or xenograft studies)? Third, what is the specific cell type, within the heterogeneous tumor cellular hierarchy, to which CLIC1 confers malignant traits to? Fourth, what is the mechanism by which CLIC1 regulates tumor growth? Addressing these knowledge gaps is key to developing a CLIC1-based rational strategy to combat malignant tumors. Here, we show that *CLIC1* is overexpressed in multiple brain cancer types, including MB. Clc1 knockout does not overly affect mouse development but suppresses MB growth in xenograft and genetically engineered mouse models. We show that CLIC1 regulates the proliferation of rapidly dividing MB cells by functionally coupling with potassium channels to control cell volume homeostasis and mitosis.

Results

CLIC1 is overexpressed in multiple human brain cancer types, including MB

To search for anion channels that regulate brain tumor malignancy, we performed bioinformatic interrogation of Gene Expression Omnibus (GEO) datasets. *CLIC1* expression is up-regulated in multiple types of primary brain tumors, including MB, GBM, pilocytic astrocytoma (grade I glioma), ependymoma, atypical teratoid rhabdoid tumor (AT/RT), and primitive

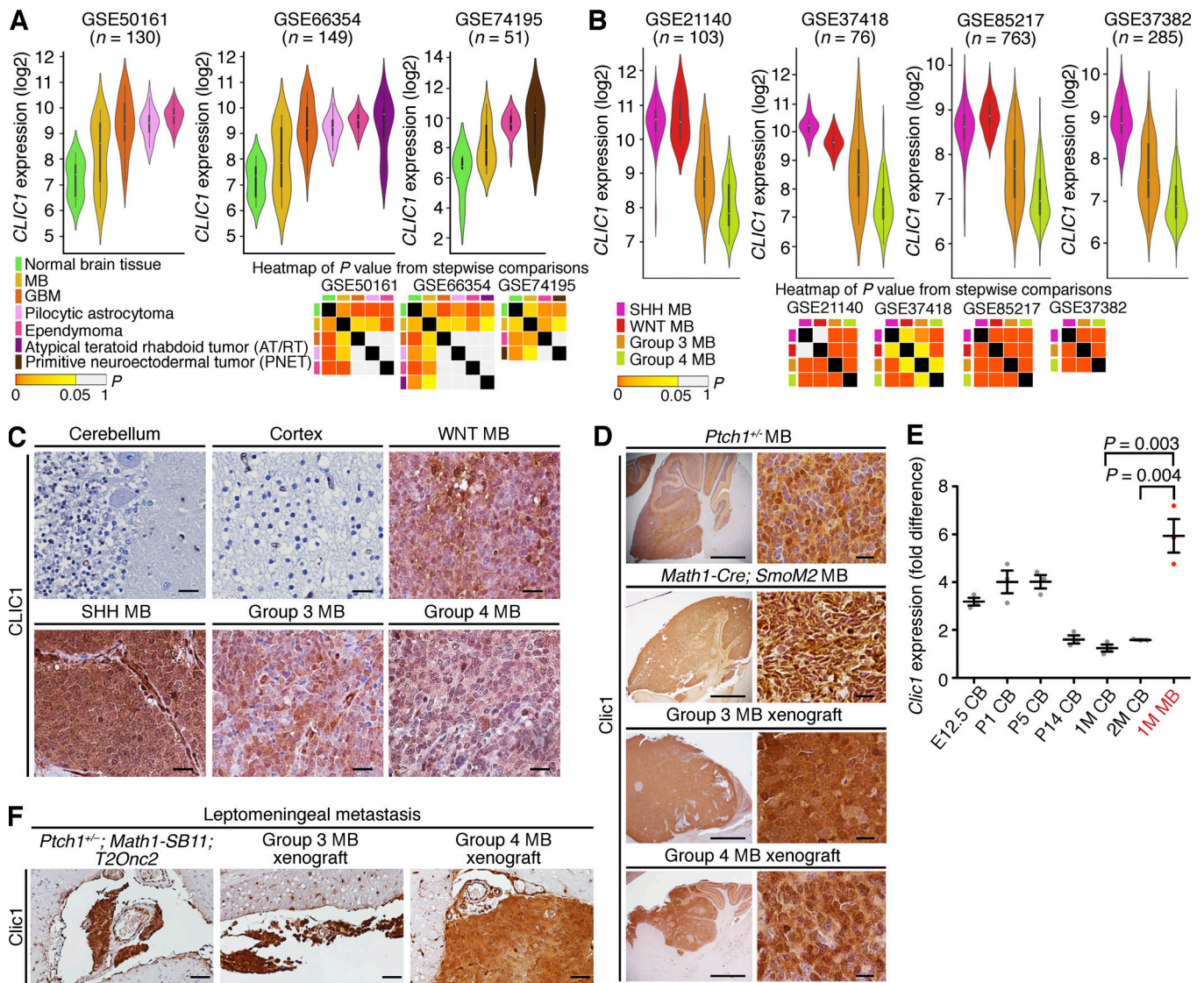


Figure 1. CLIC1 is overexpressed in human CNS cancers, including MB. (A) *CLIC1* is overexpressed in multiple types of CNS cancers, including MB, GBM, pilocytic astrocytoma, ependymoma, AT/RT, and PNET. Least significant difference or Tamhane's T2 test was used for pairwise comparison. The number of samples (*n*) are indicated in each graph. The P values from pairwise comparisons are shown in the heatmap. (B) *CLIC1* expression in MB subgroups. Least significant difference or Tamhane's T2 test was used for pairwise comparison. The number of samples (*n*) are indicated in each graph. The P values from pairwise comparisons are shown in the heatmap. (C) *CLIC1* protein is highly expressed in various subgroups of MB, while its expression is undetectable in human cerebellum or cortex tissue (*n* = 19 tumor samples; *n* = 2 nontumor samples). Scale bars = 10 μ m. (D) High *Clc1* and *CLIC1* expression is detected in SHH MB in *Ptch1*^{-/-} and *Math1-Cre*; *SmoM2* mice and group 3 and 4 MB xenograft tumors, respectively (*n* = 3 tumor samples per group; two independent experiments). Scale bars for images on the left and right column represent 5 mm and 10 μ m, respectively. (E) qPCR shows *Clc1* mRNA levels in cerebella at various developmental stages and its overexpression in the MB of *Math1-Cre*; *SmoM2* mice. E, embryonic day; M, month; P, postnatal day. Data represent mean \pm SEM. P values were obtained using unpaired two-tailed Student's *t* test (*n* = 3 samples per group; two independent experiments). (F) High *Clc1* and *CLIC1* expression is maintained in metastatic MB in *Ptch1*^{-/-}; *Math1-SB11*; *T2Onc2* mice and group 3 and 4 xenograft MB tumors, respectively (*n* = 3 samples per group; two independent experiments). Scale bars = 40 μ m.

neuroectodermal tumor (PNET; Fig. 1 A). Within MB, SHH MB, and WNT MB displayed further *CLIC1* up-regulation compared with group 3 and group 4 MB (Fig. 1 B). In a human MB tissue microarray, which included primary MB subgrouped based on DNA methylation (Cavalli et al., 2017) and normal cerebellum and cortex tissues as controls, we detected high *CLIC1* protein expression in ~58% (11 of 19) of the patient tumors, while *CLIC1* was undetectable in the nontumor controls (Fig. 1 C). *CLIC1* overexpression is recapitulated in the tumors of *Ptch1*^{-/-} and

Math1-Cre; *SmoM2* mouse models of SHH MB, as well as group 3 and 4 xenograft MB tumors (Fig. 1 D). Quantitative PCR (qPCR) analysis showed high *Clc1* expression in MB and early postnatal mouse cerebella compared with cerebella in adult mice (Fig. 1 E). Recent genomic studies showed that genetic alterations in primary MB tumors poorly overlap with those in metastatic tumors, highlighting the need to validate whether a candidate therapeutic target remains in the tumor after metastasis (Wu et al., 2012). We found that high *Clc1* and *CLIC1* expression is

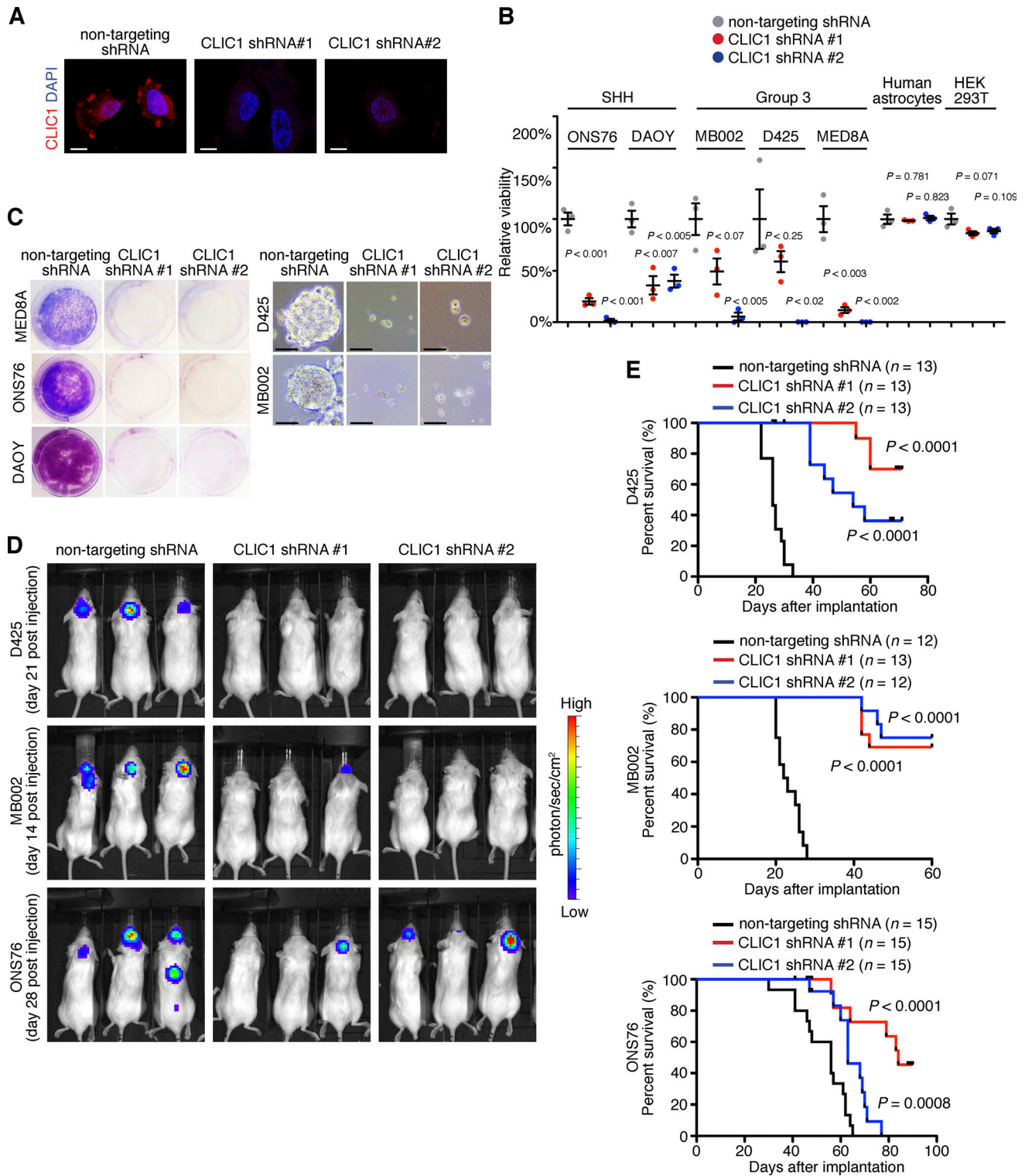


Figure 2. **CLIC1 regulates the growth of human MB in xenograft models.** (A) RNAi knockdown reduces CLIC1 protein expression in human MB cells (ONS76, two independent experiments). Scale bars = 10 μ m. (B) CLIC1 knockdown reduces the viability of human MB cells of different molecular subgroups, while it does not overtly affect the viability of human astrocyte or HEK293T cells. Data are mean \pm SEM. P values were obtained using unpaired two-tailed Student's *t* test. *n* = 7 cell lines (three biological replications per cell line, three independent experiments). (C) CLIC1 knockdown suppresses the clonogenic or sphere growth of human MB cell lines. *n* = 5 cell lines (three biological replications per cell line, two independent experiments). Left panels show wells of 6-well plates. Scale bars = 50 μ m. (D) CLIC1 knockdown inhibits the in vivo growth of xenograft MB tumors (*n* = 3 cell lines; 10–15 mice per treatment per cell line, three independent experiments). (E) Mice bearing xenografted MB with CLIC1 knockdown display significantly extended survival compared with mice bearing the control tumors (*n* = 3 independent experiments; three cell lines, 11–15 mice per treatment). P values were obtained using the log-rank test.

maintained in the metastatic MB tumors in *Ptchl1^{-/-}; Math1-SBII; T2Onc2* mice and group 3 and 4 MB xenografts, respectively (Fig. 1 F). Collectively, *CLIC1* is overexpressed in a wide spectrum of human brain tumors, including MB, and *CLIC1* overexpression is recapitulated in mouse MB models amenable to further functional investigation.

CLIC1 knockdown suppresses the growth of MB tumors in multiple xenograft models

To demonstrate the translatability of targeting *CLIC1* in human tumors, we investigated the function of *CLIC1* using human MB cell lines and xenograft models. shRNA-mediated *CLIC1* knockdown decreased *CLIC1* protein levels (Fig. 2 A and Fig. 4 A) and reduced the viability and clonogenic potential of serum-cultured ONS76, DAOY, and MED8A cells grown as monolayers (Fig. 2, B and C). *CLIC1* knockdown also suppressed the growth of SOX2⁺; NESTIN⁺ spheres of D425 and MBO02 human MB cells cultured using defined growth factors (leukemia inhibitory factor, epidermal growth factor [EGF], basic fibroblast growth factor [bFGF]) in serum-free media (Fig. 2, B and C; and Fig. S1 A). *CLIC1* knockdown did not impact the growth of human astrocytes or human embryonic kidney 293T cells (Fig. 2 B), suggesting that *CLIC1* deficiency reduces cell viability in a tumor-specific manner. Importantly, *CLIC1* knockdown suppressed the *in vivo* growth of MB tumors and extended the survival of tumor-bearing mice in multiple xenograft models (Fig. 2, D and E). These human cell line and xenograft studies demonstrate a cell-autonomous function of *CLIC1* in MB across different molecular subgroups. Interestingly, in time-matched or end-point tumors, *CLIC1* expression levels were comparable or appeared higher in *CLIC1* shRNA-treated tumors (Fig. S1, B and C). Similarly, the histology and percentages of mitotic cells were comparable between these tumors (Fig. S1, B–D). We postulate that the xenograft tumors that eventually displayed *in vivo* growth were likely from “escaper cells” with insufficient or no perturbation of *CLIC1* expression.

Clc1 knockout does not overtly affect mouse development but inhibits the proliferation of tumor cells, thereby extending the survival of SHH MB-bearing mice

Next, we asked what role *Clc1* plays in mouse development and in genetically engineered mouse models of MB. We detected *Clc1* in mouse SHH MB cells *in vivo* at various cell cycle phases (Fig. 3 A). We used CRISPR-Cas9 to generate a *Clc1* knockout mouse line by introducing a 1,458-bp deletion between introns 1 and 5, which results in the absence of *Clc1* protein (Fig. S2, A and B). *Clc1^{-/-}* mice were born at Mendelian ratio and displayed normal survival within the observed time frame of 120 d, as well as normal body weight and fertility (Fig. S2, C–F). Adult *Clc1^{+/+}* and *Clc1^{-/-}* mice displayed comparable brain morphology (Fig. S2 G). As CGNPs are the cell of origin of mouse SHH MB, we compared the proliferative capacity of CGNPs of *Clc1^{+/+}* and *Clc1^{-/-}* mice at postnatal day 7 (P7), a stage when CGNPs are rapidly dividing at the external granule neuron layer. The percentages of cycling and mitotic CGNPs are comparable between *Clc1^{+/+}* and *Clc1^{-/-}* mice (Fig. S2, H and I). Collectively, these data show that *Clc1* is dispensable for normal mouse development.

We next studied the *Math1-Cre; SmoM2* mouse model of SHH MB with and without genetic deletion of *Clc1*. Remarkably, in contrast to the lack of overt phenotype during development, *Clc1* knockout reduced MB tumor burden, suppressed tumor-associated hydrocephalus and cranium bulging, and significantly extended the survival of tumor-bearing mice (Fig. 3, B and C). MB in *Math1-Cre; SmoM2; Clc1^{-/-}* mice displayed reduced proliferation and increased apoptosis compared with the tumors in *Math1-Cre; SmoM2* mice (Fig. 3 D). A lineage-tracing study has shown that mouse SHH MB harbors a rare population of slow-cycling, Sox2⁺ brain tumor-initiating cells. The growth of SHH MB mirrors a dysregulated neurogenic program in that the Sox2⁺ cells produce Dcx⁺, transient, rapidly cycling tumor progenitor cells that subsequently generate postmitotic NeuN⁺ cells. Dcx⁺ and NeuN⁺ cells together comprise the tumor bulk (Vanner et al., 2014). We found that *Math1-Cre; SmoM2; Clc1^{-/-}* tumors displayed significantly decreased mitosis in Dcx⁺ cells (Fig. 3 E), whereas the number or percentage of mitotic Sox2⁺ cells was not altered by *Clc1* knockout (Fig. 3 F). Furthermore, we isolated and cultured Sox2⁺ cells from primary mouse MB tumors and determined that *Clc1* knockout did not overtly alter the overall growth or cell diameters (Fig. 3 G). Taken together, these data show that *Clc1* regulates rapidly dividing tumor cells, but not slow-cycling Sox2⁺ cells, in SHH MB.

CLIC1 regulates cell volume homeostasis for cell cycle progression

We next investigated the mechanism by which *CLIC1* regulates MB cell cycle progression. To achieve high resolution and define the subcellular localization of *CLIC1*, we performed *CLIC1* immunostaining followed by stimulated emission depletion (STED) superresolution imaging of human ONS76 MB cells. Differing from the potassium channels EAG2 or KCNT2 that only localizes at the plasma membrane during mitosis (Huang et al., 2012, 2015), *CLIC1* is present at the plasma membrane during both interphase and mitosis (Fig. 4 A). Furthermore, we performed total internal reflection fluorescence (TIRF) imaging to unequivocally visualize the ion channel proteins localized on the plasma membrane. Lending support to our STED imaging data, TIRF imaging showed that *CLIC1* is present on the plasma membrane during both interphase and mitosis, whereas EAG2 and KCNT2 displayed mitosis-specific localization on the plasma membrane (Fig. 4 B). To determine *CLIC1* ion channel activity, we performed perforated whole-cell patch clamp recording. We added the antibiotic gramicidin to the recording solution, which forms pores on the plasma membrane that are exclusively permeable to monovalent cations and small uncharged molecules. Gramicidin perforated-patch recording has the advantage of not altering intracellular chloride concentration and is suitable for the study of anionic channels when intracellular chloride is a variable of interest (Kyrozis and Reichling, 1995). Mitotic cells were identified based on their mitotic rounding morphology and the presence of condensed chromosomes aligned at the metaphase plate (Fig. 4 C). Currents were elicited by voltage steps from –80 mV to 80 mV in 20-mV increments. Noticeably, mitotic MB cells displayed a significantly higher level of total currents compared with cells at interphase, while *CLIC1*

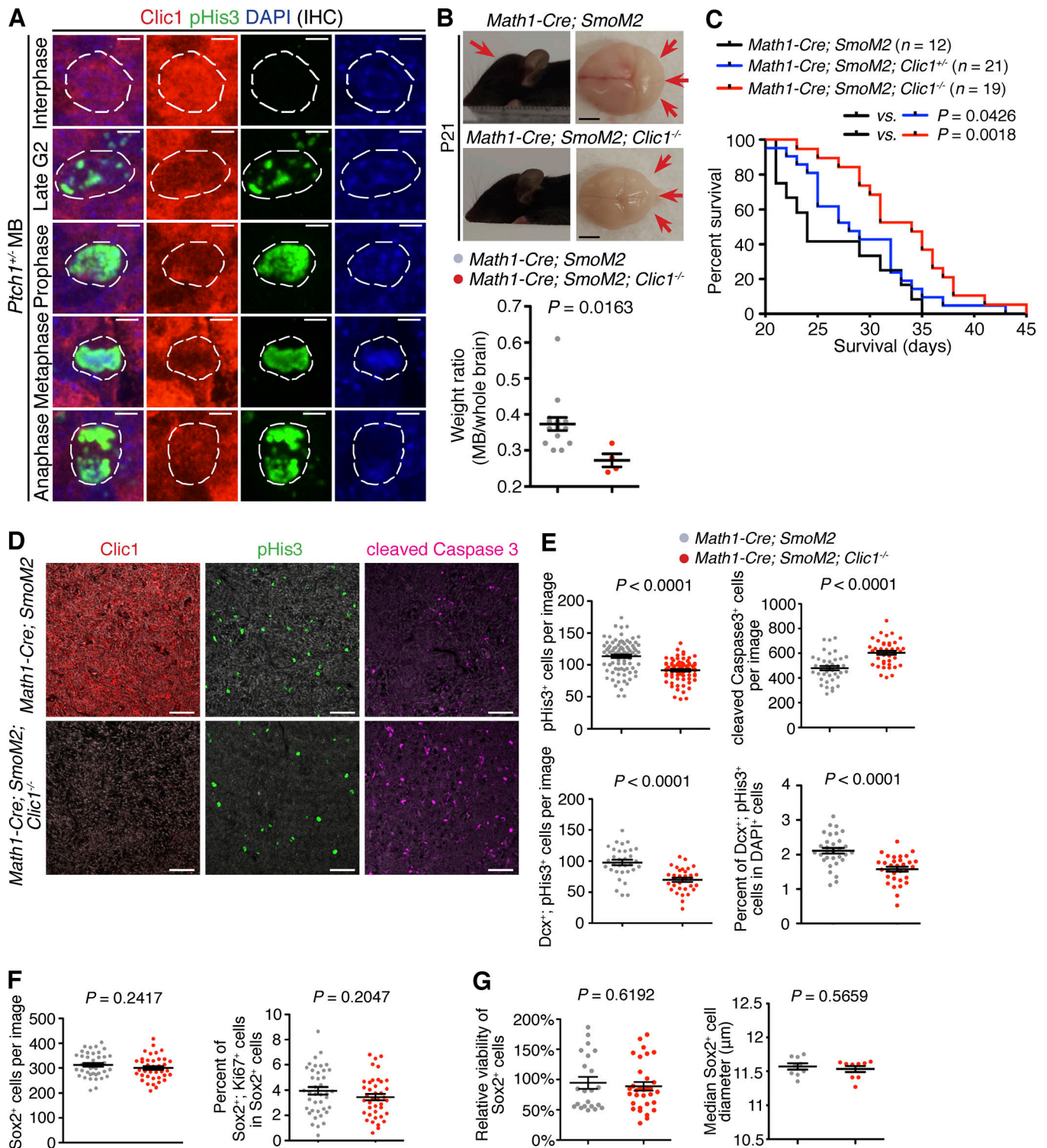


Figure 3. *Clic1* promotes the growth of mouse SHH MB by regulating the rapidly cycling tumor cells. (A) *Clic1* is detected in *Ptch1*^{+/+} MB cells in vivo at each cell cycle phase (three biological replications, two independent experiments). Scale bars = 2 μm. (B) *Clic1* knockout suppresses MB tumor burden, tumor-associated hydrocephalus, and cranium bulging in *Math1-Cre; SmoM2* mice at P21. The ratio of MB tumor weight to that of the whole brain is decreased by *Clic1* knockout. Scale bars = 5 mm. (C) *Clic1* knockout extends the survival of mice bearing *Math1-Cre; SmoM2* MB. (D) Immunohistochemical analyses of MB tumors of *Math1-Cre; SmoM2; Clic1*^{+/+} and *Math1-Cre; SmoM2; Clic1*^{-/-} mice. Scale bars = 50 μm. (E) *Clic1* knockout increases overall mitosis and decreases overall apoptosis in the tumor. *Clic1* knockdown decreases mitosis of Dcx⁺ cells. (F) *Clic1* knockout does not affect the number or percentage of Sox2⁺ cells in vivo. (G) *Clic1* knockout does not alter the growth or cell diameter of Sox2⁺ cells in vitro. For B–G, data represent mean ± SEM. n = 3 independent experiments, three to four mice per genotype. P values were obtained using an unpaired two-tailed Student’s t test (B and E–G) and log-rank test (C).

knockdown decreased the total currents during both interphase and mitosis (Fig. 4, C and D). It is important to note that we recorded total currents carried by all endogenous ion channels, including but not limited to CLIC1. The recording solutions (extracellular and internal) included potassium and chloride as the electrolytes, and the 5 mM tetraethylammonium chloride in the extracellular solution may block a substantial portion of, but not all, potassium channels. Therefore, the recorded whole-cell currents represent an aggregate of both CLIC1-mediated chloride and potassium channel-mediated potassium currents. The reduction of total currents in CLIC1 knockdown cells suggests that CLIC1 channel activity is prominent at both interphase and mitosis.

As we reported that EAG2-mediated potassium efflux is necessary for cell volume reduction and mitotic entry (Huang et al., 2012), CLIC1-mediated chloride efflux may cooperate with potassium to control cell volume and cell cycle progression. Indeed, CLIC1 knockdown significantly suppressed mitosis (Fig. 4, E and F), accompanied by an increase in cell volume, which was determined by both confocal imaging-based 3D cell volume reconstruction (Fig. 4 G) and Coulter Counter-based cell diameter measurement (Fig. 4 H). Since CLIC1, EAG2, and KCNT2 channels are present on the plasma membrane during mitosis, we asked whether these three ion channels cooperatively regulate cell volume. While ectopically expressing CLIC1, EAG2, or KCNT2 alone was sufficient to reduce the volume of COS7 cells, coexpressing two (CLIC1 and EAG2, CLIC1, and KCNT2) or three ion channels all together synergistically decreased cell volume (Fig. 4 I).

To further investigate the relationship between cell volume and cell cycle progression, we manipulated MB cell volume using various chemical compounds, including capsazepine, an activator of epithelial sodium channels, to increase sodium influx, niflumic acid to inhibit general chloride efflux, and two cholesterol synthesis inhibitors, atorvastatin and lovastatin, to suppress lipid raft formation. These pharmacological treatments resulted in a dose-dependent increase of MB cell volume (Fig. S3 A). Notably, by analyzing these same cell populations, we detected robust positive Pearson's correlation between cell volume and the percentage of MB cells at G1/G0 phase and robust negative Pearson's correlation between cell volume and the percentage of MB cells at G2/M phase (Fig. S3 B). Given that we manipulated MB cell volume using distinct pharmacological or genetic approaches, which all resulted in defects in mitotic entry, we suggest MB cell cycle progression critically depends on dynamic cell volume controls mediated by ion channel activity. Plasma membrane-localized CLIC1 conducts chloride current, CLIC1 channel activity increases during mitosis, and its deficiency results in cell swelling and defective cell cycle progression.

CLIC1 deficiency activates p38 MAPK pathway to suppress MB cell growth and is associated with uncoupling between RNA biosynthesis and cell size increase

EAG2-deficient MB cells display abnormal cell volume increase, which activates the osmolarity-sensing p38 MAPK pathway to prevent mitotic entry (Huang et al., 2012). Since CLIC1 knockdown resulted in mitotic defects and cell swelling, we asked whether the

p38 MAPK pathway is similarly activated. Indeed, CLIC1 knockdown induced the phosphorylation of p38 and its upstream kinases MKK3/6, whereas the phosphorylation level of ERK1/2 appeared unaltered (Fig. 5 A). We analyzed RNA sequencing (RNA-seq) data of nontargeting and CLIC1 shRNA-treated MB cells and identified enrichment of p38 MAPK pathway target genes upon CLIC1 knockdown (Fig. 5, A and B; and Fig. S3 C). Furthermore, we treated three MB cell lines (ONS76, MED8A, and DAOY) with nontargeting shRNA and CLIC1 shRNA and suppressed p38 MAPK activity using two structurally different kinase inhibitors (SB 203580 and SB 239063). While p38 inhibitors did not affect growth of the nontargeting shRNA treated cells, adding either p38 inhibitor profoundly rescued the growth defect caused by CLIC1 knockdown in all three MB cell lines (Fig. 5 C and Fig. S3 E). Interestingly, while p38 inhibition did not affect cell volume in control or nontargeting shRNA-treated MB cells, it partially suppressed the cell volume increase phenotype upon CLIC1 knockdown (Fig. S3 F). It is possible that inhibiting p38 activity in the presence of CLIC1 knockdown reduces cell volume through bypassing cell cycle arrest and allowing cell division. Alternatively, p38 activation may exacerbate the cell volume increase phenotype in addition to the cell swelling caused by deficient CLIC1 chloride efflux. Taken together, these data establish that CLIC1 deficiency activates the p38 MAPK pathway, which exacerbates cell swelling, and that activation of the cell volume-sensing p38 MAPK pathway is a shared mechanism that deficiency in either EAG2 or CLIC1 engages to suppress MB cell growth.

Cells scale up protein and nucleic acid biosynthesis in accordance to cell volume increase. However, aberrant cell size increase past a certain threshold results in an elevated cytoplasm/nucleus ratio, uncouples macromolecule biosynthesis, and impairs the cell cycle (Neurohr et al., 2019). We asked whether CLIC1 regulates cell volume to prevent cytoplasm dilution during cell cycle progression. To this end, we quantified the nuclear and overall cell volume. Strikingly, while the nuclear volume was not altered, CLIC1-deficient cells displayed significantly increased cell/nuclear volume ratio, suggesting that CLIC1 specifically regulates the volume of the cytoplasm (Fig. 5 D and Fig. S3 D). We performed RNA-seq and bioinformatic analysis to determine the CLIC1-dependent gene expression and signaling pathways. Gene set enrichment analysis (GSEA) identified pathways that regulate cell cycle, cell size, and cell growth (Fig. 5 E). More importantly, pathways of ribosome, RNA polymerase, Spt-Ada-Gcn5 acetyltransferase (SAGA) complex, DNA repair, proteasome, and mitochondria, all of which have been functionally linked to the oversized cells and deficient biosynthesis (Neurohr et al., 2019), are among the most altered after CLIC1 knockdown (Fig. 5 E and Fig. S4 A). Lastly, we compared the global RNA quantity of the control and CLIC1 knockdown cells. Despite an ~1.8-fold increase in cell volume (Fig. 4 G), CLIC1 knockdown MB cells express significantly decreased total RNA compared with control cells ($93.6 \pm 0.6\%$ vs. $100 \pm 0.8\%$, $P = 0.004$; Fig. 5 F), suggesting that their total RNA was diluted almost twofold relative to the control. These results suggest that CLIC1 regulates the cytoplasm/nuclear volume ratio and prevents cytoplasm dilution and indicate a role for CLIC1 in scaling RNA levels to MB cell size during cell cycle progression.

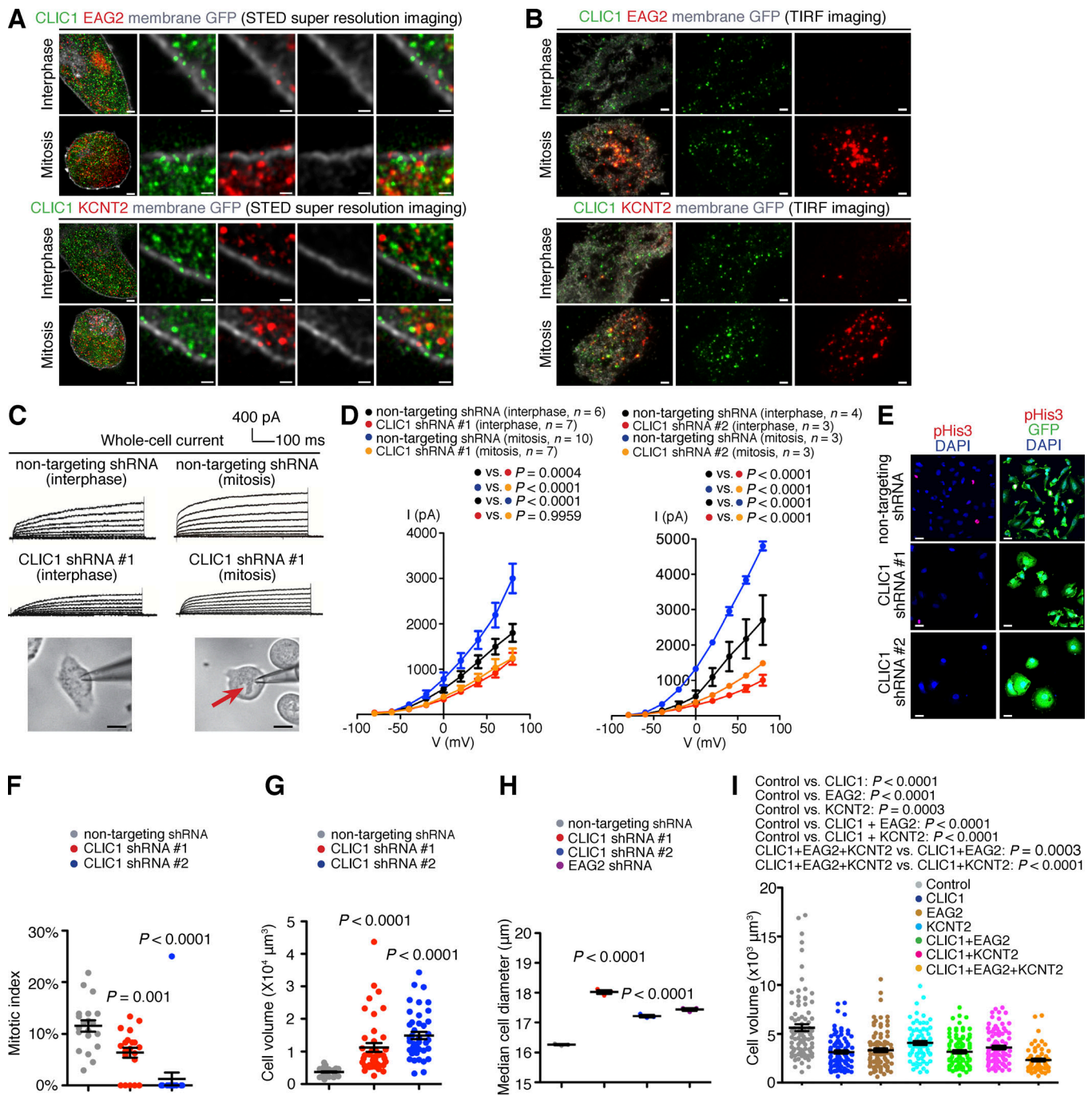


Figure 4. CLIC1 regulates cell volume and mitotic entry. (A) STED superresolution imaging of CLIC1, EAG2, and KCNT2 subcellular localization during interphase or mitosis of ONS76 cells (three biological replications, two independent experiments). Scale bars for leftmost column images represent 2 μm and 500 nm for zoomed-in images. (B) TIRF imaging of CLIC1, EAG2, and KCNT2 subcellular localization during interphase or mitosis (three biological replications, two independent experiments). Scale bars = 2 μm. (C) Representative current traces show the total currents from whole-cell recording of ONS76 cells. Currents are elicited by voltage steps from -80 mV to 80 mV in 20-mV increments. A cell at interphase or mitosis is shown with an electrode patched on the cell surface. The arrow indicates the chromosomes of a MB cell at metaphase. *n* = 2 cell lines; three biological replications per cell line, two independent experiments. Scale bars = 20 μm. (D) Current-voltage (I-V) curves show that ONS76 cells at mitosis display increased total currents compared with interphase. The total currents are significantly reduced by CLIC1 knockdown. CLIC1-dependent currents are shown by subtracting the average peak currents of the cells with CLIC1 knockdown from the average peak currents of the control cells. Data represent mean ± SEM. P values were obtained using two-way ANOVA (three biological replications, five independent experiments). (E) CLIC1 knockdown suppresses the mitosis of ONS76 cells (three biological replications, five independent experiments). Scale bars = 30 μm. (F) CLIC1 knockdown decreases the mitotic index (percentage of mitotic cells in total cells) of ONS76 cells. (G) CLIC1 knockdown increases ONS76 cell volume determined by confocal imaging and 3D reconstruction of the cells. (H) CLIC1 knockdown increases the cell diameter of DAOY cells determined by Coulter counter. (I) Quantifications show that overexpressing CLIC1, EAG2, and KCNT2 synergistically reduces the volume of COS7 cells. Data represent mean ± SEM. P values were obtained using unpaired two-tailed Student's *t* test (three biological replications, two independent experiments). For F-H, data represent mean ± SEM. P values were obtained using unpaired two-tailed Student's *t* test (three biological replications, three independent experiments).

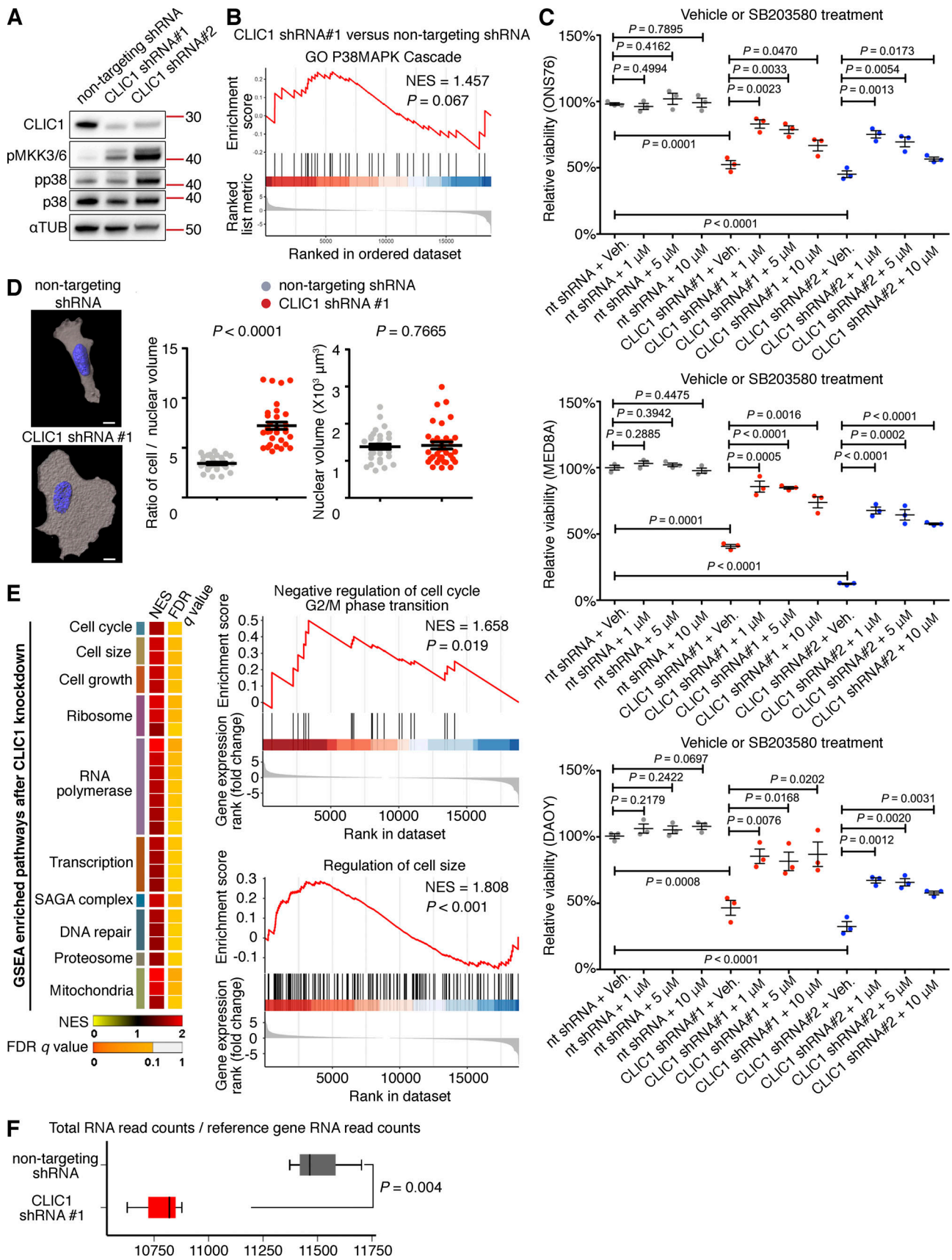


Figure 5. **CLIC1 deficiency activates p38 MAPK signaling pathway, increases the ratio of cell/nuclear volume, and decouples RNA biosynthesis from the cell size increase.** (A) Western blotting shows increased phosphorylation of MKK3/6 and p38 in the CLIC1-deficient ONS76 cells compared with the

control cells. **(B)** Gene Ontology (GO) term analysis of RNA-seq data shows enrichment of p38 MAPK pathway target genes upon CLIC1 knockdown. **(C)** Quantifications show that CLIC1 knockdown reduces the growth of human MB cell lines and SB203580 treatment rescues the growth defect. nt, non-targeting. **(D)** 3D reconstruction shows that DAOY cells with CLIC1 knockdown display an overall increase in cell size but not size of the nucleus. Soluble GFP and DAPI signal are used for 3D reconstruction and volume calculation of the cell and nucleus, respectively. Scale bars = 10 μm . **(E)** GSEA identifies altered pathways, which regulate cell cycle, cell size, cell growth, ribosome, RNA polymerase, transcription, SAGA complex, DNA repair, proteasome, and mitochondria, after CLIC1 knockdown. Enrichment plot of the pathways that regulate cell size and cell cycle G2/M phase transition are illustrated. Detailed results are shown in Fig. S4 A. FDR, false discovery rate; NES, normalized enrichment score. **(F)** Global RNA read count quantification shows significantly decreased total RNA in the CLIC1-deficient cells compared with the control cells. For A, B, E, and F, three biological replications were performed in two independent experiments. For C and D, data represent mean \pm SEM. P values were obtained using unpaired two-tailed Student's *t* test ($n = 3$ cell lines, three biological replications per cell line, and three independent experiments).

CLIC1 and EAG2 are synthetic vulnerabilities in MB cells

CLIC1 undergoes palmitoylation, a posttranslational modification that target proteins to lipid rafts (Fang et al., 2016). Cholesterol promotes CLIC1 membrane insertion and ion channel activity (Hossain et al., 2016). Since lipid rafts are cholesterol-rich microdomains on the plasma membrane, we hypothesize that lipid rafts may represent designated membrane sites where CLIC1 and EAG2 colocalize and functionally cooperate in MB cells. To study the dynamics of EAG2 and CLIC1 localization during mitosis, we first quantified EAG2 puncta and CLIC1 puncta localized at lipid rafts, and colocalization of EAG2 and CLIC1 (which we define as being within 0.2 μm apart) at lipid rafts on the plasma membrane and nonlipid raft plasma membrane, during both interphase and mitosis. While the extent of either EAG2 or CLIC1 localization at lipid rafts did not differ between interphase and mitosis (Fig. 6 A and Fig. S4 B), colocalization of EAG2 and CLIC1 on lipid rafts significantly increased at mitosis, supporting the notion that these two ion channels increase physical proximity at lipid rafts to promote potassium and chloride efflux for mitosis. We did not detect appreciable CLIC1 and KCNT2 colocalization at lipid rafts during mitosis (Fig. S4 C).

Next, we asked whether CLIC1 and EAG2 channels represent synthetic vulnerabilities in MB cells. To this end, we tested multiple concentrations of lentivirus-expressing shRNAs against CLIC1 or EAG2, either alone or in combination. We identified a specific lentiviral concentration at which single-ion-channel knockdown did not elicit discernible phenotype. However, combinatorial knockdown of CLIC1 and EAG2 induced synergistic and significant suppression of the growth of human MB cells (Fig. 6 B and Fig. S4 D). CLIC1 and EAG2 also displayed synergistic regulation of cell volume (Fig. 6 C), supporting a mechanism whereby CLIC1 and EAG2 cooperate to regulate MB cell growth by converging on cell volume control. Either single or double knockdown activated the p38 MAPK pathway (Fig. S4 E). Interestingly, we noted that p38 activation was not enhanced by comparing double- and single-channel knockdown. Since CLIC1 or EAG2 deficiency not only activated the p38 pathway but also resulted in aberrant cell volume increase and reduction of global mRNA density, a probable explanation for this is that CLIC1 and EAG2 synergize to regulate MB cell cycle progression via both p38-dependent and p38-independent mechanisms. Furthermore, these data suggest that different subgroups of MB tumors may evolve a common mechanism by which CLIC1 cooperates with potassium channels for cell cycle control. In support of this notion, our bioinformatics analysis

revealed that 10 potassium channels, including *KCNT2*, display the highest positive correlation with *CLIC1* across human MB subgroups (Fig. S5 A).

Drosophila melanogaster Eag and Clic channels cooperate to regulate brain tumor growth in vivo

Drosophila represents a powerful genetically tractable model to study brain tumor biology. During *Drosophila* larval brain development, neuroblasts (neural stem cells) proliferate to self-renew and generate neural progenitor cells, neurons, and glia. Timely cell cycle entry and exit is key to brain development, and aberrant cell cycle progression leads to brain tumorigenesis (Homem and Knoblich, 2012). *insc-Gal4* is a genetic driver active in the proliferative neuroblast and progenitor cells. *insc-Gal4*-driven expression of the basic helix-loop-helix oncogene *Dpn* results in uncontrolled neuroblast self-renewal (Zhu et al., 2012), which mimics neural stem cell- or progenitor-derived human brain tumors, including MB. Using this model, we previously identified the potassium channel Eag as a critical regulator of the growth of *Drosophila* brain tumors (Huang et al., 2015). Here, we first asked whether the *Drosophila* chloride intracellular channel (Clic) plays an evolutionarily conserved role in governing the proliferation of brain tumor cells. A previous study has identified two hypomorphic alleles of *Clic*, *Clic^{EYO4209}* and *Clic^{G0472}*, in which transposon insertions abrogated transcript expression (Bhandari et al., 2012). As *Clic* is located on the X chromosome, we generated male brain tumor-bearing larvae with either one of the two *Clic* mutations. We used the *insc-Gal4* to express mCD8-GFP that labels cell membranes and performed confocal imaging to quantify the volume of tumor tissues. We also performed immunostaining to quantify the numbers of neuroblasts and neural progenitor cells (*Dpn*⁺) and glia cells (*Repo*⁺). Both hypomorphic mutations reduced the number of *Dpn*⁺; pHis3⁺ mitotic neuroblast and neural progenitor cells and decreased the volume of mCD8-GFP⁺ tumor tissue (Fig. 6 D). As a control, global *Clic* deficiency in the *Clic^{EYO4209}* or *Clic^{G0472}* mutants (without brain tumors) did not result in consistent alteration of the numbers of *Dpn*⁺ or *Repo*⁺ cells of the brain lobes and ventral nerve cord (VNC; Fig. S5 B), highlighting a heightened dependency on *Clic* in brain tumors compared with normal brains.

Having established the essential role of *Clic*, we then modeled our combinatorial RNA interference (RNAi) experiments in human MB cells and asked whether *Clic* and *Eag* functionally cooperate to regulate *Drosophila* brain tumor growth. We selected specific RNAi lines such that single *Clic* or *Eag* RNAi was

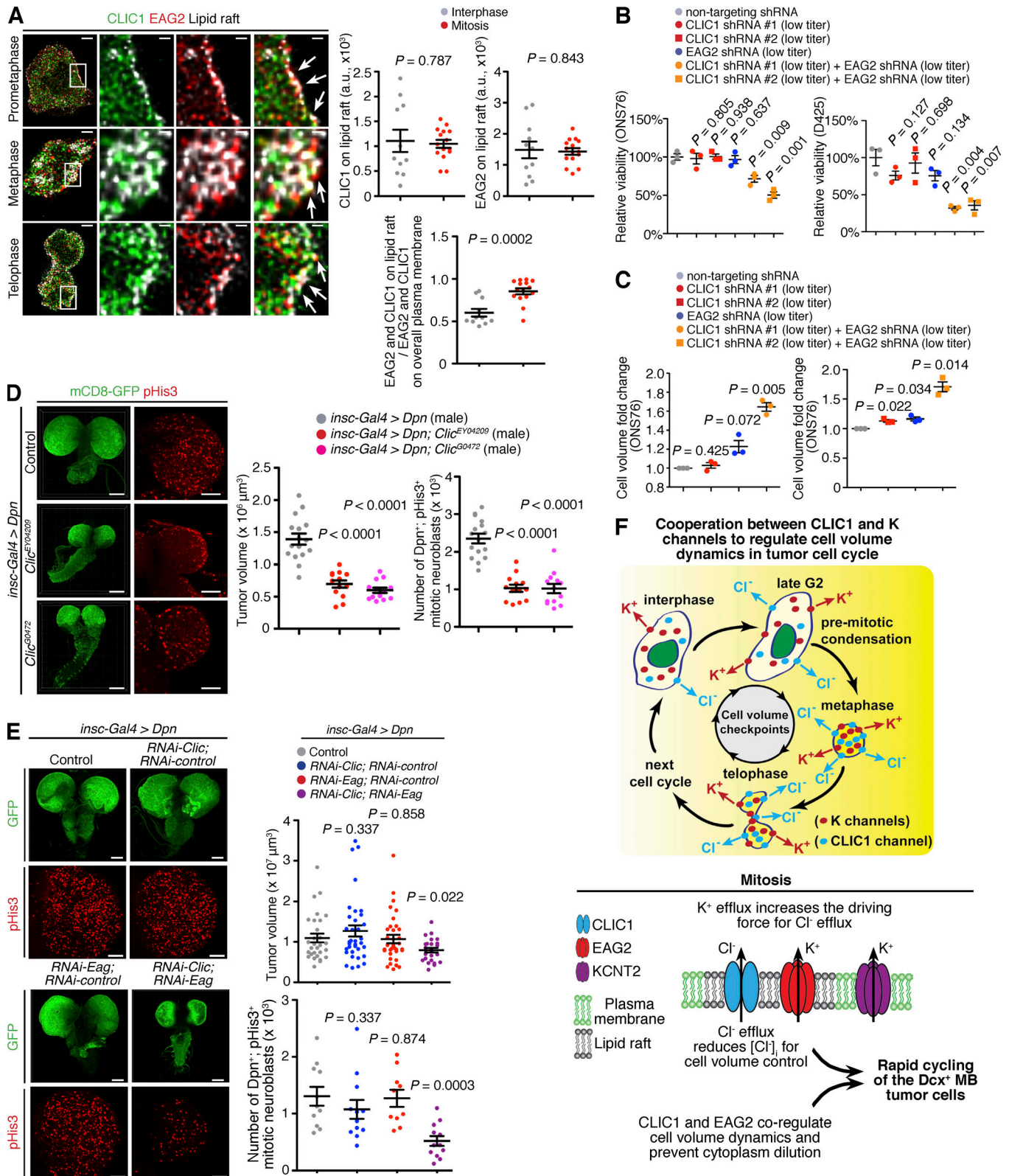


Figure 6. **CLIC1/EAG2 and Clic/Eag functionally couple to regulate the growth of human MB cells and *Drosophila* brain tumors, respectively.** (A) CLIC1 and EAG2 colocalize at lipid rafts during mitosis of ONS76 cells. Quantifications of the immunofluorescence signals show that the localization of EAG2 or CLIC1 on lipid rafts does not differ between interphase and mitosis, while colocalization of both EAG2 and CLIC1 on lipid rafts significantly increases at mitosis. The arrows denote where there is colocalization of EAG2 and CLIC1 on the lipid rafts (white). Scale bars for leftmost column images are 3 μm and 600 nm for zoomed-in images. (B) Combinatorial RNAi knockdown of CLIC1 and EAG2 display synergistic effect in decreasing the viability of human MB cells. (C) Combinatorial RNAi knockdown of CLIC1 and EAG2 display synergistic effect in increasing the volume of human MB cells. (D) *insc-Gal4*-driven Dpn

expression leads to uncontrolled proliferation, which results in expanded brain and VNC volume and tumorigenesis. Hypomorphic *Clic* mutation (*Clic^{EYO4209}* or *Clic^{G0472}*) suppresses mitosis and decreases the volume of Dpn-overexpressing tissue. The Dpn-overexpressing cells are labeled by *insc-Gal4*-driven mCD8-GFP (plasma membrane-tagged GFP). As *Clic* is on the X chromosome, monoallelic mutation is hemizygous in male. Scale bars for left and right column images represent 100 μm and 60 μm , respectively. **(E)** Representative images of the brains and VNCs of *insc-Gal4 > Dpn* larvae show that single RNAi against *Clic* or *Eag* does not affect tumor growth, whereas combinatorial RNAi knockdown reduces the volume of mCD8⁺ Dpn-overexpressing tissue, as well as the number of Dpn⁺; pHis3⁺ mitotic tumor cells. Scale bars for top and bottom row images represent 100 μm and 50 μm , respectively. **(F)** A model for CLIC1 to regulate MB cell cycle and the rationale for targeting CLIC1 and potassium channels to suppress MB. At mitosis, Cl⁻ efflux through CLIC1 prevents excessive cell swelling and cytoplasmic dilution. K⁺ efflux mediated by potassium channels, such as EAG2 and KCNT2, makes MB cell membrane potential more negative, hence increasing the driving force for Cl⁻ efflux through CLIC1. The concurrent efflux of Cl⁻ and K⁺ promotes cell volume reduction to facilitate mitotic entry and is a prerequisite for cell cycle progression. CLIC1 and EAG2 channels functionally couple to ensure mitotic success of MB cells. In SHH MB, blocking the activity of cooperative ion channels suppresses malignancy through inhibiting the proliferation of rapidly dividing Dcx⁺ tumor cells. For A–E, data are mean \pm SEM. P values were obtained using unpaired two-tailed Student's *t* test. For A, three biological replications were performed in three independent experiments. For B and C, three biological replications were performed per cell line in eight independent experiments. For D and E, 10 to 30 fly larvae brains per genotype were analyzed in three independent experiments.

unable to cause tumor suppression, likely due to insufficient gene knockdown. Notably, we observed robust synergism when we combined the RNAi of both *Clic* and *Eag* (Fig. 6 E). As a control, either single or double ion channel knockdown did not elicit difference in the number of Dpn⁺ neuroblast and progenitor cells or the volume of *insc-Gal4*-driven mCD8-GFP-labeled neuroblast lineage in the nontumor-bearing larvae (Fig. S5 C). Collectively, our *Drosophila* data demonstrate a dependency on *Clic* in oncogenically transformed cells and establish *Clic* and potassium channel cooperation as an evolutionarily conserved mechanism that fuels malignant brain tumor growth in vivo.

Discussion

An integrative cross-species platform to identify ion channels as dependencies of brain tumor

MB is one of the most prevalent childhood brain cancers. As a large class of cell surface proteins and drug targets for a variety of human diseases, ion channels in brain tumors are underexplored. By bioinformatic interrogation of large Cancer Genome Atlas datasets, we found that *CLIC1* is overexpressed in multiple human CNS cancer types, including MB (Fig. 1). Using xenograft models, we demonstrated that CLIC1 knockdown suppressed the growth of MBs across molecular subgroups (Fig. 2). By generating *Clic1* knockout mice and studying genetically engineered mouse models, we showed that *Clic1* is dispensable for normal mouse development, whereas *Clic1* knockout suppressed tumor growth in a mouse model of SHH MB (Fig. 3). Mechanistically, we discovered that CLIC1-dependent ion channel activity increases at mitosis (Fig. 4). We showed that CLIC1 deficiency activates the cell volume-sensing p38 MAPK pathway to suppress MB cell growth and uncovered that CLIC1 regulates MB growth through controlling the molecular machineries that converge on regulation of cell size and RNA biosynthesis to prevent cytoplasm dilution (Fig. 5). Furthermore, we identified lipid rafts as the plasma membrane microdomains where CLIC1 and EAG2 enrich during mitosis (Fig. 6) and demonstrated that combinatorial targeting of CLIC1/EAG2 and *Clic/Eag* suppresses the growth of human MB cells in vitro and *Drosophila* brain tumors in vivo, respectively (Fig. 6). Our studies highlight the utility of a cross-species platform to identify evolutionarily conserved tumor dependencies, establish CLIC1 and EAG2 channels as synthetic vulnerabilities in MB, and reveal the

mechanism of action by which CLIC1 regulates tumorigenesis (Fig. 6 F).

CLIC1 in cancer

We discovered previously unreported CLIC1 overexpression in multiple types of primary brain tumors, including MB, pilocytic astrocytoma, ependymoma, AT/RT, and PNET. This widespread alteration of *CLIC1* expression in human tumors indicates that CLIC1 may regulate fundamental aspects of malignant cells. We propose that CLIC1 functionally couples with potassium channels to control cell volume oscillation to facilitate tumor cell cycle progression. *Clic1*^{-/-} mice are viable and fertile, without overt phenotypes, highlighting the value of CLIC1 as a cancer therapeutic target. We note that CLIC1 may play additional roles in the cytosol or at intracellular organelles to regulate tumor growth. CLIC1 may also function in nontumoral cells, such as macrophage or microglia, to influence tumor progression. It is intriguing that CLIC1 knockdown resulted in stronger growth suppression in human MB xenograft tumors compared with genetically deleting *Clic1* in the *Math1-Cre; SmoM2* mouse SHH MB. We consider several possible reasons. First, constitutive global *Clic1* knockout in mice may allow compensatory mechanisms to reduce tumor dependency on *Clic1*. Second, MB is a highly heterogeneous disease. The *Math1-Cre; SmoM2* mouse model of SHH MB may not represent the human MB tumors we used in the xenograft studies. Third, MB tumors that arise in mouse and human may develop species-specific dependency on *Clic1* and CLIC1, respectively.

Functionally coupled ion channels as regulators for tumor growth

Ion channels cooperate to regulate biological processes. For example, activating the calcium-permeating TRPV4 channel results in increased activity of the calcium-activated chloride channel TMEM16A, which controls chloride flux to regulate the volume of choroid plexus epithelial cells. This cooperation between TRPV4 and TMEM16A is facilitated by physical interaction (Takayama et al., 2014). TRPV4 and calcium-activate potassium channel SK3 cocluster in the caveolae of endothelial cells to regulate vasodilation (Goedicke-Fritz et al., 2015). Superresolution imaging demonstrated various classes of ion channels intimately associate with each other to form signaling macromolecular complexes in neurons (Zhang et al., 2016). We

speculate that a network of ion channels temporally and spatially enriches to membrane microdomains and functionally couple to regulate cancer cell behavior, including, but not limited to, mitosis. Identifying the components of such ion channel networks will reveal ample new therapeutic opportunities.

Therapeutically targeting CLIC1 in cancer

We identified that the US Food and Drug Administration-approved antipsychotic drug thioridazine is an EAG2 channel blocker, which displayed therapeutic efficacy in treating MB in mice and a patient (Huang et al., 2015). IAA-94, which inhibits CLIC1, decreased the capacity for colorectal cancer cells to regulate volume during cell migration (Wang et al., 2012). However, the high concentration required for IAA-94 to function and its effect on CLIC1–CLIC6 preclude its use as a CLIC1-specific agent for cancer treatment. A specific and potent CLIC1 inhibitor is needed for further therapeutic development. As the structure of soluble CLIC1 is known, rational design of CLIC1-interacting small molecules or peptides may offer new avenues to blocking CLIC1 function. Alternatively, high-throughput screening of agents that either antagonize CLIC1 channel activity or prevent its membrane trafficking may lead to the development of CLIC1-specific targeted therapy. A combination therapy targeting CLIC1 and its functionally coupled potassium channels (e.g., EAG2 in MB) should maximize the tumor-suppressive effect. Leveraging tumor dependency on overexpressed ion channels such as CLIC1 represents a novel approach to effectively treat devastating cancers such as MB.

Materials and methods

Fly stocks

The following fly stocks were used: *insc-Gal4* (Bloomington stock number 8751), *Gal4* inserted in the *insc* promoter to drive gene expression in the neuroblast lineage; *UAS-Dpn* (Yuh Nung Jan laboratory, University of California, San Francisco, San Francisco, CA), *UAS*-driving expression of *Dpn*; *Clic^{EY04209}* (Bloomington stock number 15725), hypomorphic allele of *Clic*; *Clic^{G0472}* (Bloomington stock number 12267), hypomorphic allele of *Clic*; *RNAi-Clic* (Vienna Drosophila Resource Center stock number 105975), *UAS*-driving expression of *RNAi* against *Clic*; *RNAi-control* (Bloomington stock number 35786), *UAS*-driving *RNAi* expression against a scrambled sequence; *RNAi-Eag* (Vienna Drosophila Resource Center stock numbers 31678 and 9126), *UAS*-driving *RNAi* expression against *Eag*; *UAS-mCD8-GFP* (Bloomington stock number 32189), *UAS*-driving expression of *mCD8-GFP*.

Fly culture, *Drosophila* immunostaining, confocal microscopy, and image quantifications

All larvae and flies were cultured at 25°C, aside from those involving the *Clic* hypomorphic mutants, which were cultured at room temperature. Randomly selected third-instar larvae were dissected in PBS, fixed in 4% formaldehyde for 20 min at room temperature, and incubated with primary antibody overnight at 4°C and secondary antibody for 2 h at room temperature. Primary antibodies were chicken anti-GFP (1:1,000; Aves Labs),

rabbit anti-Dpn (1:500; Yuh Nung Jan laboratory), mouse anti-Repo (1:100; Developmental Studies Hybridoma Bank) and rat (1:200; Abcam) or rabbit (1:500; Abcam) anti-phosphorylated Histone H3 (Ser10). Secondary antibodies conjugated to Alexa Fluor 488, 555, or 647 (Cell Signaling Technologies) were used at 1:500. Images were acquired with a 20× objective on a Leica SP8 confocal microscope or a Quorum spinning disk confocal equipped with a Leica DMI8 microscope and Photometric Prime 95B camera, with a Z-step size of 5 μm. Tissue volume (*insc-Gal4*-driven *mCD8-GFP*) or *Dpn* and *Repo* was determined by Imaris software (v9.2) after 3D reconstruction of z-stack confocal images using the Surfaces function (with surface detail smoothing = 1 μm, manual thresholding based on absolute intensity, background subtraction, and filtering based on signal intensity mean). Mitotic cells (pHis3⁺), *Dpn*, and *Repo* cells in the nontumor brains were quantified using the Spots quantification function on Imaris (with an estimated diameter = 4 μm, manual thresholding, background subtraction, filtering, and manual deletion of nonspecific spots). To quantify the number of *Dpn*⁺; pHis3⁺ double-positive cells, a MATLAB extension on Imaris (Find Spots close to Surfaces, with a distance threshold determined by the average of manual distance measurements between the spots and surfaces of interest) was used. To assess the survival of adult *Drosophila*, the resulting progeny classes from each cross were scored. Crosses and scoring were performed three independent times.

Mouse lines, immunohistochemistry, and quantification

Ptch1^{+/-}, *Math1-Cre*, *SmoM2* mice were previously described and cited in the text. *Clic1^{-/-}* mice were generated at The Centre for Phenogenomics by injecting Cas9 mRNA and two guide RNAs with spacer sequences 5'-TTAGATAGAGGCTTAGTGAA-3' and 5'-CCAGTACCCAATTAATAAGC-3'. This resulted in a 1,458-bp deletion in chromosome 17 (35,052,089–35,053,546), which spans from intron 1–2 to intron 4–5 in the *Clic1* gene. The common name for this allele is *Clic1_{em2}del*. The official nomenclature is *C57BL / 6N-Clic1^{em2T_{cp}}*. All procedures were performed in compliance with the Animals for Research Act of Ontario and the Guidelines of the Canadian Council on Animal Care. The Centre for Phenogenomics Animal Care Committee reviewed and approved our protocol 19-0288H. All strains were backcrossed at least eight generations, and littermates were used as controls for all experiments.

Immunohistochemistry, immunofluorescence, and H&E staining were performed on paraffin-embedded tissue sections. The primary antibodies were mouse anti-CLIC1 (1:50; Santa Cruz Biotechnologies), rabbit anti-Sox2 (1:100; Abcam), rabbit anti-Dcx (1:100; Abcam), mouse anti-phospho-Histone H3 (1:1,000; Cell Signaling Technologies), rabbit anti-cleaved Caspase 3 (1:200; Cell Signaling Technologies), rabbit anti-Pax6 (1:100; BioLegend), and rabbit anti-Ki67 (1:100; Abcam). Images were acquired with a Leica SP8 Lightning Confocal (DMI6000) microscope. The numbers of Pax6⁺, Ki67⁺, Sox2⁺, pHis3⁺, or cleaved-caspase3⁺ cells were quantified using the “Spots” function on Imaris software with an estimated diameter of 2.5–4.5 μm, manual thresholding, background subtraction, and filtering. *Dcx* volume was determined through the “Surface” function in

Imaris after 3D reconstruction of z-stack confocal images (with smoothing level of 0.5 μm , manual thresholding, background subtraction, and filtering based on signal intensity mean). To quantify the number of Dcx⁺; pHis3⁺ double-positive cells, a MATLAB extension on Imaris: Find Spots close to Surfaces with a distance threshold determined by the average of manual distance measurements between the spots and surfaces of interest, was used.

The group 3 xenograft MB used for CLIC1 immunohistochemistry in Fig. 1 is Med-411FH, which is a MYC amplified group 3 xenograft obtained from the Brain Tumor Resource Laboratory, and profiled using genome-wide methylation arrays at our institution and reported (Brabetz et al., 2018). The group 4 xenograft MB used for CLIC1 immunohistochemistry in Fig. 1 is DMB006, which was previously reported (Pei et al., 2016).

Mouse Sox2⁺ MB cells were isolated from *Math1-cre; SmoM2* and *Math1-cre; SmoM2; Clc1^{-/-}* mice and cultured as previously described (Huang et al., 2010). Briefly, primary MB tumors were mechanically dissociated by repetitive pipetting using ice-cold PBS without Mg²⁺ and Ca²⁺, followed by treatment using 50% Accutase diluted in PBS. The dissociated cells were cultured on a plate surface coated with poly-L-ornithine and laminin using Neurocult NS-A Basal media supplemented with 2 mmol/liter L-glutamine, N2 supplement, B27 supplement, 75 $\mu\text{g}/\text{ml}$ BSA, 2 $\mu\text{g}/\text{ml}$ Heparin, 10 ng/ml bFGF, and 10 ng/ml human EGF.

Human MB tissue microarray

Primary MB samples subgrouped using DNA methylation were used to assemble the tissue microarray (Cavalli et al., 2017). Three representative cores per sample were used along with normal cerebellum and cortex tissues as controls. Tissue samples (sections) were deparaffinized and rehydrated through an alcohol gradient to water for antigen retrieval in 10 mM citrate buffer, pH 6.0, in a rice cooker. The mouse anti-CLIC1 antibody (1:50; Santa Cruz Biotechnologies) was incubated overnight at 4°C, and the anti-rabbit HRP step was performed with 1-h incubation at room temperature. The 3'-diaminobenzidine color reaction was developed at room temperature and stopped after 5 min. The slides were then counterstained with hematoxylin. Tissue sections were imaged using a 3DHitech Panoramic 250 Flash II Slide Scanner.

Cell culture, clonogenic and cell viability assays, immunofluorescence staining, and drug inhibition experiments

DAOY and MED8A human MB cell lines were cultured using DMEM with 10% FBS. The ONS76 human MB cell line was cultured using RPMI with 10% FBS and supplemented with sodium pyruvate. D425 and MB002 human MB cell lines were cultured using 50:50 neural basal medium and DMEM/F12 supplemented with nonessential amino acids, sodium pyruvate, Hepes, glutamine, B27, heparin, 25 ng/ml human leukemia inhibitory factor (LIF), 25 ng/ml bFGF, and 25 ng/ml human EGF without addition of serum. All cell lines were regularly checked for mycoplasma infections and treated with Plasmocin (Invivogen) when infection was noted. No cell lines are listed in the database of commonly misidentified cell lines maintained by the International

Cell Line Authentication Committee and National Center for Biotechnology Information BioSample.

To determine the clonogenic potential of brain tumor cells, cells were infected with lentivirus for 4 d and replated at clonal density (150 cells/ml of culture medium) into 60-mm plates. Cell colonies were stained with 0.05% crystal violet 7–10 d after seeding. Representative results from three independent experiments were shown. Cell viabilities were determined using CellTiter 96 AQueous One Solution Cell Proliferation Assay (Promega) after plating (500–1,000 cells per well). For the nonadherent D425 or MB002 cell lines, the cells were plated in serial dilutions (ranging from 2,000 to 3 cells per well) on nonadherent 96-well plates in six biological replicates. 1 wk after plating, the CellTiter 96 AQueous One Solution Cell Proliferation Assay was performed to measure cell viabilities on a spectrophotometer.

To perform the double knockdown (CLIC1 and EAG2), MB cells were plated in 96-well plates at a density of 500–1,000 cells per well. Multiple concentrations of the lentivirus, which encode shRNA targeting CLIC1 or EAG2, either alone or in combinations were added to the wells. Each well received an equal virus titer (in the single knockdown conditions, control shRNA was added equalize viral titer). The relative viabilities were determined using CellTiter 96 AQueous One Solution Cell Proliferation Assay (Promega) after lentivirus treatment as described (in three biological replicates).

To perform immunofluorescence staining, cells were grown on 1-mm coverslips (or 1.5 mm for superresolution and TIRF imaging), fixed in 4% formaldehyde at 4°C overnight, and incubated with primary antibody overnight at 4°C and secondary antibody for 1 h at room temperature. For nonadherent lines, the staining was performed in 0.5-ml tubes with constant nutation. The primary antibodies were chicken anti-GFP (1:2,000; Living Colors), rabbit anti-EAG2 (1:1,000; Alomone), rabbit anti-KCNT2 (1:500; Novus), mouse anti-CLIC1 (1:250; Developmental Studies Hybridoma Bank), rat anti-phospho-Histone H3 (1:10,000; Abcam), rabbit anti-Sox2 (1:1,000; Abcam), and rabbit anti-Nestin (1:500; Abcam). Secondary antibodies conjugated to Alexa Fluor 488, 555, and 647 (Cell Signaling Technologies) were used at 1:1,000, and those conjugated to Alexa Fluor 405, 594, and 532 (Thermo Fisher) were used at 1:2,000. For STED superresolution staining, images were acquired using a Leica SP8 Lightning Confocal (DMI6000) with STED 3X microscope using Hybrid Detector (HyD) detectors and processed using Huygens Professional deconvolution software. The concentrations for the primary and secondary antibodies were increased 5 \times and 3 \times , respectively. DAPI or TO-PRO3 was used to visualize DNA. For TIRF imaging, cells were grown and stained as previously described but remained unmounted. TIRF images were acquired using a Zeiss Elyra PS1 (Axio Observer Z1) microscope with an Andor iXon3 885 (SIM) detector and processed using Imaris software.

Lipid rafts were labeled using the Molecular Probes Vybrant Lipid Raft Labeling Kits–Alexa Fluor 555, followed by staining with a goat anti-cholera toxin B (1:200; Fitzgerald Antibodies) to amplify the signal. Confocal and STED superresolution images were acquired with a Leica SP8 Lightning Confocal (DMI6000)

with STED 3X microscope using HyD detectors. For super-resolution imaging, a 93× (glycerol immersion) objective was used using constant-wave STED 594- and 660-nm depletion lasers with gating. Image deconvolution for the lipid rafts experiment was performed using the Leica Lightning deconvolution software. Image deconvolution for superresolution images was performed using Huygens Profession Software with a STED function.

Analysis and quantification for the lipid rafts experiment was performed using Imaris in a multistep process. To define the localization of EAG2 and CLIC1, we first quantified the immunofluorescence signals defined as spots using Imaris software on lipid rafts (lipid raft label⁺). The Spots function was used to create a 3D reconstruction and to quantify the number of EAG2, CLIC1, or KCNT2, with background subtraction and filtering using intensity mean. The Surfaces function was used to create a 3D reconstruction of the lipid rafts or membrane GFP. Two MATLAB extensions were used with manual thresholding: Colocalize Spots to quantify the total EAG2 + CLIC1 and KCNT2 + CLIC1 colocalization and Find Spots Close to Surface to determine the number of each EAG2, CLIC1, KCNT2, EAG2 + CLIC1, or KCNT2 + CLIC1 that are on either lipid rafts or membrane GFP. A colocalization channel was built using the “Coloc” function on Imaris to determine the are covered by both lipid rafts (lipid raft label⁺) and nonlipid raft plasma membrane (membrane GFP⁺; lipid raft label⁻), and this was 3D-reconstructed using the Surfaces function. Then MATLAB: Find Spots Close to Surface was used to determine the number of EAG2, CLIC1, KCNT2, EAG2 + CLIC1, or KCNT2 + CLIC1 that are both on lipid rafts and membrane GFP. The relative number of colocalized EAG2 + CLIC1 and KCNT2 + CLIC1 on lipid rafts was determined using the following equation: EAG2 + CLIC1 spots close to lipid rafts + mGFP surface/total EAG2 + CLIC1 spots close to mGFP surface.

To determine cell volume, we expressed soluble GFP in MB cells and performed serial confocal imaging. We acquired the image stacks with a z-step size at 1 μm per optical slice using a 63× 1.4-NA oil lens throughout the entire thickness of the cells. All subsequent image processing was conducted with Imaris 9.2 software and volume was measured using the Surfaces function as previously described above. For cell diameter measurements, cells were plated at a density of 60,000 cells per well in 6-well plates and treated as described for knockdown or pharmacological experiments. Cell diameter measurements were taken 3–4 d after infection or drug treatment. Cells were resuspended using trypsin and incubated in isotonic solution, and diameter was measured using the Multisizer 4 Coulter Counter (Beckman-Coulter) using standard protocols and a threshold of 12–60 μm. All experiments were repeated three times.

p38 MAPK inhibitors SB203580 and SB239063 were obtained from Tocris (catalog numbers 1202 and 1962) and dissolved in DMSO as 10 mM stock. Indicated concentrations of SB203580 and SB239063 were added on the second day post lentivirus infection (following the replacing virus-containing medium with virus-free new medium). Cell viability assays were performed at day 5–10 after infection. Cell diameter measurements were obtained using the Multisizer 4 Coulter Counter

(Beckman-Coulter) using standard protocols and a threshold of 12–30 μm.

Drug treatment, cell diameter measurement, and cell cycle analysis by propidium iodide staining

Atorvastatin, lovastatin, capsazepine, and niflumic acid were obtained from Tocris (catalog numbers 3776, 1530, 0464, and 4112, respectively) and dissolved in DMSO to the following stock concentrations: atorvastatin, 10 mM; lovastatin, 10 mM; capsazepine, 30 mM; and niflumic acid, 50 mM. ONS76 MB cells were plated and treated with the indicated concentration of drugs and collected 3 d after for cell diameter measurement and propidium iodide staining. Cell diameter measurements were obtained using the Multisizer 4 Coulter Counter (Beckman-Coulter) using standard protocols and a threshold of 12–30 μm.

For cell cycle analysis, resuspended MB cells were fixed overnight in 80% ethanol at 4°C. Fixed cells were incubated in 2 mg/ml bovine RNase IIA (Sigma) for 5 min at room temperature. Cells were stained in 0.1 mg/ml propidium iodide solution (Life Technologies) in HBSS (Gibco) containing 0.6% Triton X-100 (Bio Basic) for 30 min at room temperature, protected from light. Stained cells were resuspended in HBSS containing 10 mM HEPES-NaOH, pH 7.2, 2% FBS (Gibco), and 10 mM Na₃N, then filtered through cell-strainer caps (Falcon) into FACS tubes immediately before flow cytometry measurement. Data were collected on a Becton Dickinson (BD) LSRFortessa cell analyzer, with acquisition software BD FACSDiva v.8.0. Subsequent cell cycle analysis was performed on FlowJo 10 using the Watson Pragmatic algorithm cell cycle platform.

Western blotting

Total protein was extracted using a lysis buffer containing 50 mM HEPES, pH 7.4, 150 mM NaCl, 1% NP-40, 1 mM dithiothreitol, 1 mM EDTA supplemented with Complete Protease Inhibitor Cocktail (Roche). Protein lysate samples, 25 μg each, were resolved on 4–12% Bis-Tris gels using 3-(N-morpholino) propanesulfonic acid (MOPS) buffer (Invitrogen) and transferred onto a polyvinylidene fluoride membrane (Amersham Biosciences) using a buffer containing 25 mM Tris base, pH 8.3, 192 mM glycine, and 20% methanol for 2 h at 200 V at 4°C. Western blot assays were performed using the appropriate dilution of primary antibody in TBS supplemented with 0.1% Tween-20 and 0.5% milk or 0.5% BSA. Immunoreactive bands were visualized using HRP-conjugated secondary antibodies (Cell Signaling Technologies), followed by chemiluminescence with ECL-plus Western Blotting Detection System (Amersham). Chemiluminescence was imaged and analyzed using Molecular Imager@VersaDoc MP4000 system (Bio-Rad). The primary antibodies used were mouse anti-CLIC1 (1:500; Santa Cruz Biotechnologies), mouse-anti-αTubulin (1:10,000; Sigma), rabbit-anti-phospho-AKT (Thr308; 1:1,000; Cell Signaling Technologies), rabbit-anti-phospho-p38 (Thr180/Tyr182; 1:1,000; Cell Signaling Technologies), rabbit-anti-phospho-MKK3 (Ser189)/MKK6 (Ser207; 1:1,000; Cell Signaling Technologies), rabbit anti-phospho-ERK1/2 (Thr202/Tyr204; 1:1,000; Cell Signaling Technologies), and rabbit-anti-p38 (1:1,000; Cell Signaling

Technologies). Average fold change of protein level from three independent experiments were indicated below the corresponding protein bands.

RNA extraction, reverse transcription, and real-time RT-PCR

For mouse cerebellum and MB tissues, total RNAs were extracted using TRIzol (Thermo Fisher) and cleaned up with a RNeasy Plus Mini kit (Qiagen). 150 ng to 1 µg RNA was reverse transcribed to cDNA using the SensiFAST cDNA synthesis kit (BIOLINE). All DNA and RNA concentrations were measured by a NanoDrop 1000 Spectrophotometer. Real-time detection and quantification of cDNAs were performed with the Vii7 Cyclor (Applied Biosystems). qPCR was performed in a 15-µl reaction mixture using SYBR Green qPCR Supermixes (Applied Biosystems). 40 cycles of amplification were performed according to manufacturer's instructions. Fluorescence data were collected at annealing stages and real-time analysis performed with Vii7 System Software. Ct values were determined with automatically set baseline and manually adjusted fluorescence threshold. Gene expressions were normalized with that of a control housekeeping gene and analyzed using the $\Delta\Delta C_t$ method. All experiments were repeated three times.

The following primers were used (h, human; m, mouse): hCLIC1, 5'-TTCAAACCCAGCACTCAATG-3' (forward), 5'-TCAGCACTGGTTTCATCCAC-3' (reverse); hGAPDH, 5'-CTCCTGCACCACCAACTGCT-3' (forward), 5'-GGGCCATCCACAGTCTTCTG-3' (reverse); mClc1, 5'-ACTCAAACCCAGCCCTCAAT-3' (forward), 5'-CGCTGGTTTCATCCACTTCT-3' (reverse); and mGapdh, 5'-TTCACCACATGGAGAAGGC-3' (forward), 5'-GGCATGGACTGTGGTCATGA-3' (reverse).

RNA-seq

Total RNAs were extracted from DAOY and ONS76 cells (control and CLIC1-knockdown treated) using TRIzol (Thermo Fisher) and cleaned up with an RNeasy Plus Mini kit (Qiagen). Total RNA (genomic DNA-depleted) samples were sent to The Hospital for Sick Children TCAG Sequencing Facility for poly(A) library prep and sequenced on an Illumina HiSeq 2500 platform with a target of 30 million reads per sample.

Lentivirus-mediated shRNA study

Human pLKO.1 lentiviral shRNA target gene set against *CLIC1* and pLKO.1-TRC-control vector were obtained from Open Biosystems. Virus infections were performed within antibiotics-free culture medium for 24 h. The *CLIC1* shRNA mature antisense sequences are 5'-TTCAGCACTGGTTTCATCCAC-3' (#1) and 5'-TCAACGGTGGTAACATTGAAG-3' (#2). The *EAG2* shRNA mature antisense sequence is 5'-ATATTATTCTTGAGTCGCAGC-3'.

Xenograft and in vivo bioluminescence imaging

Tumor cells with firefly luciferase-expressing reporter

MB cells were transduced with a lentiviral vector containing firefly luciferase under the control of the spleen focus-forming virus promoter. Cells were screened for infection efficiency by treatment with luciferin (D-luciferin potassium salt; Gold Biotechnology) in vitro and examination by the Xenogen IVIS Lumina System. More than 95% of cells were infected.

Surgical procedure for implantation of tumor cells

6–8-wk-old female *NOD scid gamma/J#5557* immunodeficient mice were used for xenograft experiments. The mice were housed under aseptic conditions, which included filtered air and sterilized food, water, bedding, and cages. Age-matched mice with the same sex (females) were randomly assigned to experimental groups. There were no specific inclusion or exclusion criteria. Mice were anesthetized using gaseous isoflurane and immobilized in a stereotaxic head frame. The skull of the mouse was exposed, and a small opening was made using a sterile dental drill (Precision Guide) at 2 mm lateral and 3 mm posterior to lambda. At this location, 2×10^5 MB002, D425, or ONS76 cells in 2–3 µl culture media were slowly injected (over 2 min) 2 mm deep to the surface of the skull using a 26G Hamilton syringe. All procedures were performed under sterile conditions.

In vivo bioluminescence monitoring

In vivo bioluminescence imaging was performed using the Xenogen IVIS Lumina System coupled to LivingImage software for data acquisition. Mice were anesthetized using gaseous isoflurane and imaged 10 min after intraperitoneal injection of luciferin. Signal intensity was quantified within a region of interest over the head defined by the LivingImage software.

Electrophysiology

ONS76 cells were seeded on coverslips for 48–72 h and voltage-clamped in perforated whole-cell configurations at room temperature using an Axopatch 200B amplifier (Molecular Devices). Cells were placed in an electrophysiology recording chamber and bathed with (in mM) 130 N-methyl-D-glucamine chloride, 2 MgCl₂, 2 CaCl₂, 10 Hepes, 10 glucose, and 5 tetraethylammonium chloride, pH 7.4, with NMDG. The internal (pipette) solution consisted of (in mM): 145 KCl, 1 MgCl₂, and 10 Hepes, pH 7.25, with KOH. 2.5 µg/ml Gramicidin was added to the internal solution before each recording experiment. Patch electrodes (borosilicate glass) with a resistance of ~4 MΩ were used. Pipette and whole-cell capacitance were compensated. The voltage protocol consisted of 600-ms pulses from -80 mV to +80 mV (20-mV voltage steps). The data were filtered at 2 kHz, digitized at 10 kHz, and analyzed using pClamp10 (Molecular Devices). Current-voltage curves were generated by plotting peak current amplitude at different voltages. Quantified data were graphed using GraphPad Prism 5.

Bioinformatic studies

Data availability statement

The RNA-seq raw data of this study are available from the Sequence Read Archive repository (accession numbers PRJNA517338 and PRJNA592377).

The public datasets used in this study are available from the GEO repository (accession numbers GSE50161, GSE66354, GSE74195, GSE21140, GSE37418, GSE85217, GSE37382, GSE40593, and GSE15209).

Code availability statement

The code for bioinformatics analysis can be acquired from https://github.com/SiyiWanggou/CLIC1_in_Medulloblastoma.

Datasets and data processing

The gene expression datasets GSE50161, GSE66354, GSE74195, GSE21140, GSE37418, GSE85217, and GSE37382 were acquired from the GEO.

GSE50161 is gene expression data of nontumoral brain tissue, MB, GBM, pilocytic astrocytoma, and ependymoma. The gene expression profiles were generated by Affymetrix HG-U133plus2 chips.

GSE66354 is gene expression data of nontumoral brain tissue, MB, GBM, pilocytic astrocytoma, ependymoma, and AT/RT. The gene expression profiles were generated by Affymetrix HG-U133plus2 chips.

GSE74195 is gene expression data of PNET, MB, ependymoma, and normal brain tissue from the cerebellum. The gene expression profiles were generated by HG-U133plus2Chips.

GSE21140 is gene expression data of MB from different molecular subgroups. The gene expression profiles were generated by Affymetrix Human Exon 1.0 ST Array platform.

GSE37418 is gene expression data of MB from different molecular subgroups.

GSE85217 includes a total of 763 MB samples, representing four molecular subgroups.

GSE37382 is a dataset that includes MB samples from molecular subgroups of SHH, WNT, and group 4.

For GEO microarray datasets, background subtraction, normalization, and expression summarization of raw files were performed using the Robust Multi-array Average algorithm in R and Bioconductor packages *affy* and *beadarray*.

Statistics for *CLIC1* expression comparison in high-throughput datasets

Equality of variances was tested by Leven's test. For equal variances assumed data, one-way ANOVA was used for mean comparison and least significant difference test was used for stepwise multiple comparison of P values. For equal variances not assumed data, we used Welch's test for mean comparison and Tamhane's T2 test for stepwise multiple comparison of P values.

Determining *CLIC1* correlated ion channel genes in MB

The GSE85217 dataset was processed for detecting *CLIC1* correlated ion channel genes in MB. We used the R package *psych* to calculate matrix correlations and probabilities of all the gene pairs in the dataset. Gene pairs with *r* value >0.3 and false discovery rate value <0.05 were identified as significant. Finally, we regained a matrix containing 763 MB patients and 48 *CLIC1* significantly correlated ion channel genes. The hierarchical clustering with agglomerative average linkage targeting the new matrixes was performed with the R/ConsensusClusterPlus package and the heatmap were generated via R/Heatmap function by Z score.

RNA-seq analysis of *CLIC1* knockdown in DAOY and ONS76 cell lines

The adapters of fastq files were trimmed by TrimGalore. The clean paired-end reads were mapped to GRCh38 genome reference using HISAT2. StringTie was used for transcripts assembly and quantification. Differential expression was determined by DEseq2. Differentially expressed genes with an adjusted P value (false discovery rate) < 0.1 and fold change >2 (or <0.5) were accepted as significant.

Enrichment analysis

For differentially expressed genes in RNA-seq, we performed enrichment analysis targeting on pathways in Gene Ontology and Kyoto Encyclopedia of Genes and Genomes. GSEA was used for enrichment analysis via the R package *clusterprofiler*. Pathways with a false discovery rate <0.1 were considered as enriched. The GSEA enrichment plots were generated by R package *enrichplot*.

Total RNA estimation

The total RNA from RNA-seq in each DAOY sample was determined by combining the read counts of all genes. The estimated total RNA was generated by dividing total RNA-seq read counts with average read counts of reference genes. Housekeeping genes, including *ABCB7*, *ABCD3*, *ABCF1*, *ABCF2*, *MFSD3*, *MFSD5*, *SLC25A28*, *SLC25A38*, *SLC25A39*, *SLC30A5*, *SLC35B1*, *SLC39A7*, and *SLC46A3*, were used as reference genes.

Statistical analyses

No statistical methods were used to predetermine sample sizes. The statistical analyses were done afterwards without interim data analysis. No data points were excluded. A two-tailed Student's *t* test was performed for comparison between two groups of samples. Two-way ANOVA analyses were used to assess significance of multiple data points. The Kaplan–Meier estimator and GraphPad Prism software were used to generate survival curves. Differences between survival curves were calculated using a log-rank test. The data meet the assumptions of the tests. The variance has been tested in each group of the data, and the variance is similar among genotypes. Data distribution was assumed to be normal, but this was not formally tested. All data were collected and processed randomly. Each experiment has been successfully reproduced at least three times and was performed on multiple days. All data are expressed as mean ± SEM. We considered a P value <0.05 to be statistically significant.

Online supplemental material

Fig. S1 shows characterizations of human MB cell lines and xenograft tumors. Fig. S2 shows that *Clic1* knockout does not affect mouse development, survival, or body weight. Fig. S3 shows the analyses of cell volume, cell cycle, and the p38 MAPK pathway of human MB cells. Fig. S4 shows the subcellular localization of *CLIC1* and *KCNT2* and identification of *CLIC1*-correlated ion channels in human MB tumors. Fig. S5 shows that *Clic* mutations or RNAi knockdown of *Clic*, *Eag*, or both does not elicit overt phenotype in *Drosophila* larval neuroblast, progenitor, or glia cells.

Acknowledgments

We are grateful to Lily Jan and Yuh Nung Jan for their support during the beginning phase of this project and Susan Younger for her mentoring on *Drosophila* genetics. The Dpn antibody was a gift from the Jan laboratory. We thank Paul Paroutis and Kimberly Lau at the SickKids Imaging Facility for their help with confocal imaging and image analysis. We thank Chi-chung Hui and Peter Dirks for constructive suggestions on the project and their laboratories for

technical support. We thank all Huang laboratory members for critical reading of the manuscript. X. Huang acknowledges love and support from Lucas Huang and Liam Huang.

This work is supported by the SickKids Foundation, the Arthur and Sonia Labatt Brain Tumour Research Centre, Garron Family Cancer Centre, b.r.a.i.n.child, Meagan's Walk, the Natural Sciences and Engineering Research Council of Canada (Discovery Grant RGPIN-2016-05644), the Ontario Institute for Cancer Research (Translational Research Initiative), the US Department of Defense Peer Reviewed Cancer Research Program (Career Development Award CA160264), the Canadian Institutes of Health Research (Project Grants 377122 and 406569), and the Sontag Foundation (Distinguished Scientist Award to X. Huang). X. Huang is a Catalyst Scholar of The Hospital for Sick Children and Canada Research Chair in Cancer Biophysics.

Author contributions: Conception of project: X. Huang; Experimental design, data acquisition and interpretation: M.A. Francisco, S. Wanggou, J.J. Fan, W. Dong, X. Chen, A. Momin, N. Abeysundara, H-K. Min, J. Chan, R. McAdam, M. Sia, R.J. Pusong, S. Liu, N. Patel, V. Ramaswamy, N. Kijima, L-Y. Wang, Y. Song, R. Kafri, M.D. Taylor, X. Li, and X. Huang; Manuscript writing: M.A. Francisco, J.J. Fan, and X. Huang.

Disclosures: Dr. Ramaswamy reported personal fees from AstraZeneca outside the submitted work. No other disclosures were reported.

Submitted: 31 May 2019

Revised: 27 November 2019

Accepted: 16 January 2020

References

Al Khamici, H., L.J. Brown, K.R. Hossain, A.L. Hudson, A.A. Sinclair-Burton, J.P. Ng, E.L. Daniel, J.E. Hare, B.A. Cornell, P.M. Curmi, et al. 2015. Members of the chloride intracellular ion channel protein family demonstrate glutaredoxin-like enzymatic activity. *PLoS One*. 10: e115699. <https://doi.org/10.1371/journal.pone.0115699>

Bhandari, P., J.S. Hill, S.P. Farris, B. Costin, I. Martin, C.L. Chan, J.T. Alaimo, J.C. Bettinger, A.G. Davies, M.F. Miles, and M. Grotewiel. 2012. Chloride intracellular channels modulate acute ethanol behaviors in *Drosophila*, *Caenorhabditis elegans* and mice. *Genes Brain Behav.* 11:387-397. <https://doi.org/10.1111/j.1601-183X.2012.00765.x>

Boucrot, E., and T. Kirchhausen. 2008. Mammalian cells change volume during mitosis. *PLoS One*. 3:e1477. <https://doi.org/10.1371/journal.pone.0001477>

Brabetz, S., S.E.S. Leary, S.N. Gröbner, M.W. Nakamoto, H. Şeker-Cin, E.J. Garzia, B. Cole, A.D. Strand, K.L. Bloom, V. Hovestadt, et al. 2018. A biobank of patient-derived pediatric brain tumor models. *Nat. Med.* 24: 1752-1761. <https://doi.org/10.1038/s41591-018-0207-3>

Cavalli, F.M.G., M. Remke, L. Rampasek, J. Peacock, D.J.H. Shih, B. Luu, L. Garzia, J. Torchia, C. Nor, A.S. Morrissy, et al. 2017. Intertumoral Heterogeneity within Medulloblastoma Subgroups. *Cancer Cell*. 31: 737-754.e6. <https://doi.org/10.1016/j.ccell.2017.05.005>

Chen, C.D., C.S. Wang, Y.H. Huang, K.Y. Chien, Y. Liang, W.J. Chen, and K.H. Lin. 2007. Overexpression of CLIC1 in human gastric carcinoma and its clinicopathological significance. *Proteomics*. 7:155-167. <https://doi.org/10.1002/pmic.200600663>

Chernet, B.T., and M. Levin. 2014. Transmembrane voltage potential of somatic cells controls oncogene-mediated tumorigenesis at long-range. *Oncotarget*. 5:3287-3306. <https://doi.org/10.18632/oncotarget.1935>

Clare, J.J. 2010. Targeting ion channels for drug discovery. *Discov. Med.* 9: 253-260.

Ding, Q., M. Li, X. Wu, L. Zhang, W. Wu, Q. Ding, H. Weng, X. Wang, and Y. Liu. 2015. CLIC1 overexpression is associated with poor prognosis in

gallbladder cancer. *Tumour Biol.* 36:193-198. <https://doi.org/10.1007/s13277-014-2606-5>

Edelstein, K., B.J. Spiegler, S. Fung, T. Panzarella, D.J. Mabbott, N. Jewitt, N.M. D'Agostino, W.P. Mason, E. Bouffet, U. Tabori, et al. 2011. Early aging in adult survivors of childhood medulloblastoma: long-term neurocognitive, functional, and physical outcomes. *Neuro-oncol.* 13: 536-545. <https://doi.org/10.1093/neuonc/nor015>

Fang, C., X. Zhang, L. Zhang, X. Gao, P. Yang, and H. Lu. 2016. Identification of Palmitoylated Transitional Endoplasmic Reticulum ATPase by Proteomic Technique and Pan Antipalmitoylation Antibody. *J. Proteome Res.* 15:956-962. <https://doi.org/10.1021/acs.jproteome.5b00979>

Frangé, P., C. Alapetite, G. Gaboriaud, D. Bours, J.M. Zucker, M. Zerach, H. Brisse, M. Chevignard, V. Mosseri, E. Bouffet, and F. Doz. 2009. From childhood to adulthood: long-term outcome of medulloblastoma patients. The Institut Curie experience (1980-2000). *J. Neurooncol.* 95: 271-279. <https://doi.org/10.1007/s11060-009-9927-z>

Goedicke-Fritz, S., A. Kaistha, M. Kacic, S. Markert, A. Hofmeister, C. Busch, S. Bänfer, R. Jacob, I. Grgic, and J. Hoyer. 2015. Evidence for functional and dynamic microcompartmentation of Cav-1/TRPV4/K(Ca) in caveolae of endothelial cells. *Eur. J. Cell Biol.* 94:391-400. <https://doi.org/10.1016/j.jecb.2015.06.002>

Goodrich, L.V., L. Milenković, K.M. Higgins, and M.P. Scott. 1997. Altered neural cell fates and medulloblastoma in mouse patched mutants. *Science*. 277:1109-1113. <https://doi.org/10.1126/science.277.5329.1109>

Habela, C.W., and H. Sontheimer. 2007. Cytoplasmic volume condensation is an integral part of mitosis. *Cell Cycle*. 6:1613-1620. <https://doi.org/10.4161/cc.6.13.4357>

Hille, B. 2001. Ion Channels of Excitable Membranes. Sinauer, Sunderland, MA. 814 pp.

Homem, C.C., and J.A. Knoblich. 2012. *Drosophila* neuroblasts: a model for stem cell biology. *Development*. 139:4297-4310. <https://doi.org/10.1242/dev.080515>

Hossain, K.R., H. Al Khamici, S.A. Holt, and S.M. Valenzuela. 2016. Cholesterol Promotes Interaction of the Protein CLIC1 with Phospholipid Monolayers at the Air-Water Interface. *Membranes (Basel)*. 6:15. <https://doi.org/10.3390/membranes6010015>

Huang, X., T. Ketova, Y. Litingtung, and C. Chiang. 2010. Isolation, Enrichment, and Maintenance of Medulloblastoma Stem Cells. *J. Vis. Exp.* (43). <https://doi.org/10.3791/2086>

Huang, X., A.M. Dubuc, R. Hashizume, J. Berg, Y. He, J. Wang, C. Chiang, M.K. Cooper, P.A. Northcott, M.D. Taylor, et al. 2012. Voltage-gated potassium channel EAG2 controls mitotic entry and tumor growth in medulloblastoma via regulating cell volume dynamics. *Genes Dev.* 26: 1780-1796. <https://doi.org/10.1101/gad.193789.112>

Huang, X., Y. He, A.M. Dubuc, R. Hashizume, W. Zhang, J. Reimand, H. Yang, T.A. Wang, S.J. Stehbens, S. Younger, et al. 2015. EAG2 potassium channel with evolutionarily conserved function as a brain tumor target. *Nat. Neurosci.* 18:1236-1246. <https://doi.org/10.1038/nn.4088>

Jia, N., S. Dong, G. Zhao, H. Gao, X. Li, and H. Zhang. 2016. CLIC1 overexpression is associated with poor prognosis in pancreatic ductal adenocarcinomas. *J. Cancer Res. Ther.* 12:892-896. <https://doi.org/10.4103/0973-1482.154057>

Jiang, L., K. Salao, H. Li, J.M. Rybicka, R.M. Yates, X.W. Luo, X.X. Shi, T. Kuffner, V.W. Tsai, Y. Husaini, et al. 2012. Intracellular chloride channel protein CLIC1 regulates macrophage function through modulation of phagosomal acidification. *J. Cell Sci.* 125:5479-5488. <https://doi.org/10.1242/jcs.110072>

Kyrozis, A., and D.B. Reichling. 1995. Perforated-patch recording with gramicidin avoids artifactual changes in intracellular chloride concentration. *J. Neurosci. Methods*. 57:27-35. [https://doi.org/10.1016/0165-0270\(94\)00116-X](https://doi.org/10.1016/0165-0270(94)00116-X)

Littler, D.R., S.J. Harrop, S.C. Goodchild, J.M. Phang, A.V. Mynott, L. Jiang, S.M. Valenzuela, M. Mazzanti, L.J. Brown, S.N. Breit, and P.M. Curmi. 2010. The enigma of the CLIC proteins: Ion channels, redox proteins, enzymes, scaffolding proteins? *FEBS Lett.* 584:2093-2101. <https://doi.org/10.1016/j.febslet.2010.01.027>

Lu, J., Q. Dong, B. Zhang, X. Wang, B. Ye, F. Zhang, X. Song, G. Gao, J. Mu, Z. Wang, et al. 2015. Chloride intracellular channel 1 (CLIC1) is activated and functions as an oncogene in pancreatic cancer. *Med. Oncol.* 32:616. <https://doi.org/10.1007/s12032-015-0616-9>

Ma, P.F., J.Q. Chen, Z. Wang, J.L. Liu, and B.P. Li. 2012. Function of chloride intracellular channel 1 in gastric cancer cells. *World J. Gastroenterol.* 18: 3070-3080. <https://doi.org/10.3748/wjg.v18.i24.3070>

Neurohr, G.E., R.L. Terry, J. Lengefeld, M. Bonney, G.P. Brittingham, F. Moretto, T.P. Miettinen, L.P. Vaites, L.M. Soares, J.A. Paulo, et al. 2019. Excessive

- Cell Growth Causes Cytoplasm Dilution And Contributes to Senescence. *Cell*. 176:1083–1097.e18. <https://doi.org/10.1016/j.cell.2019.01.018>
- Novarino, G., C. Fabrizi, R. Tonini, M.A. Denti, F. Malchiodi-Albedi, G.M. Lauro, B. Sacchetti, S. Paradisi, A. Ferroni, P.M. Curmi, et al. 2004. Involvement of the intracellular ion channel CLIC1 in microglia-mediated beta-amyloid-induced neurotoxicity. *J. Neurosci.* 24: 5322–5330. <https://doi.org/10.1523/JNEUROSCI.1170-04.2004>
- Pei, Y., K.W. Liu, J. Wang, A. Garancher, R. Tao, L.A. Esparza, D.L. Maier, Y.T. Udaka, N. Murad, S. Morrissy, et al. 2016. HDAC and PI3K Antagonists Cooperate to Inhibit Growth of MYC-Driven Medulloblastoma. *Cancer Cell*. 29:311–323. <https://doi.org/10.1016/j.ccell.2016.02.011>
- Qiu, M.R., L. Jiang, K.I. Matthaei, S.M. Schoenwaelder, T. Kuffner, P. Mangin, J.E. Joseph, J. Low, D. Connor, S.M. Valenzuela, et al. 2010. Generation and characterization of mice with null mutation of the chloride intracellular channel 1 gene. *Genesis*. 48:127–136.
- Rudin, C.M., C.L. Hann, J. Laterra, R.L. Yauch, C.A. Callahan, L. Fu, T. Holcomb, J. Stinson, S.E. Gould, B. Coleman, et al. 2009. Treatment of medulloblastoma with hedgehog pathway inhibitor GDC-0449. *N. Engl. J. Med.* 361:1173–1178. <https://doi.org/10.1056/NEJMoa0902903>
- Salao, K., L. Jiang, H. Li, V.W. Tsai, Y. Husaini, P.M. Curmi, L.J. Brown, D.A. Brown, and S.N. Breit. 2016. CLIC1 regulates dendritic cell antigen processing and presentation by modulating phagosome acidification and proteolysis. *Biol. Open*. 5:620–630. <https://doi.org/10.1242/bio.018119>
- Schüller, U., V.M. Heine, J. Mao, A.T. Kho, A.K. Dillon, Y.G. Han, E. Huillard, T. Sun, A.H. Ligon, Y. Qian, et al. 2008. Acquisition of granule neuron precursor identity is a critical determinant of progenitor cell competence to form Shh-induced medulloblastoma. *Cancer Cell*. 14:123–134. <https://doi.org/10.1016/j.ccr.2008.07.005>
- Setti, M., N. Savalli, D. Osti, C. Richichi, M. Angelini, P. Prescia, L. Fornasari, M.S. Carro, M. Mazzanti, and G. Pelicci. 2013. Functional role of CLIC1 ion channel in glioblastoma-derived stem/progenitor cells. *J. Natl. Cancer Inst.* 105:1644–1655. <https://doi.org/10.1093/jnci/djt278>
- Singh, H., and R.H. Ashley. 2006. Redox regulation of CLIC1 by cysteine residues associated with the putative channel pore. *Biophys. J.* 90: 1628–1638. <https://doi.org/10.1529/biophysj.105.072678>
- Takayama, Y., K. Shibasaki, Y. Suzuki, A. Yamanaka, and M. Tominaga. 2014. Modulation of water efflux through functional interaction between TRPV4 and TMEM16A/anoctamin 1. *FASEB J.* 28:2238–2248. <https://doi.org/10.1096/fj.13-243436>
- Taylor, M.D., P.A. Northcott, A. Korshunov, M. Remke, Y.J. Cho, S.C. Clifford, C.G. Eberhart, D.W. Parsons, S. Rutkowski, A. Gajjar, et al. 2012. Molecular subgroups of medulloblastoma: the current consensus. *Acta Neuropathol.* 123:465–472. <https://doi.org/10.1007/s00401-011-0922-z>
- Tulk, B.M., S. Kapadia, and J.C. Edwards. 2002. CLIC1 inserts from the aqueous phase into phospholipid membranes, where it functions as an anion channel. *Am. J. Physiol. Cell Physiol.* 282:C1103–C1112. <https://doi.org/10.1152/ajpcell.00402.2001>
- Ulmasov, B., J. Bruno, K. Oshima, Y.W. Cheng, S.P. Holly, L.V. Parise, T.M. Egan, and J.C. Edwards. 2017. CLIC1 null mice demonstrate a role for CLIC1 in macrophage superoxide production and tissue injury. *Physiol. Rep.* 5:e13169. <https://doi.org/10.14814/phy2.13169>
- Valenzuela, S.M., D.K. Martin, S.B. Por, J.M. Robbins, K. Warton, M.R. Bootcov, P.R. Schofield, T.J. Campbell, and S.N. Breit. 1997. Molecular cloning and expression of a chloride ion channel of cell nuclei. *J. Biol. Chem.* 272:12575–12582. <https://doi.org/10.1074/jbc.272.19.12575>
- Valenzuela, S.M., H. Alkhamici, L.J. Brown, O.C. Almond, S.C. Goodchild, S. Carne, P.M. Curmi, S.A. Holt, and B.A. Cornell. 2013. Regulation of the membrane insertion and conductance activity of the metamorphic chloride intracellular channel protein CLIC1 by cholesterol. *PLoS One*. 8: e56948. <https://doi.org/10.1371/journal.pone.0056948>
- Vanner, R.J., M. Remke, M. Gallo, H.J. Selvadurai, F. Coutinho, L. Lee, M. Kushida, R. Head, S. Morrissy, X. Zhu, et al. 2014. Quiescent sox2(+) cells drive hierarchical growth and relapse in sonic hedgehog subgroup medulloblastoma. *Cancer Cell*. 26:33–47. <https://doi.org/10.1016/j.ccr.2014.05.005>
- Wang, W., X. Xu, W. Wang, W. Shao, L. Li, W. Yin, L. Xiu, M. Mo, J. Zhao, Q. He, and J. He. 2011. The expression and clinical significance of CLIC1 and HSP27 in lung adenocarcinoma. *Tumour Biol.* 32:1199–1208. <https://doi.org/10.1007/s13277-011-0223-0>
- Wang, P., C. Zhang, P. Yu, B. Tang, T. Liu, H. Cui, and J. Xu. 2012. Regulation of colon cancer cell migration and invasion by CLIC1-mediated RVD. *Mol. Cell. Biochem.* 365:313–321. <https://doi.org/10.1007/s11010-012-1271-5>
- Warton, K., R. Tonini, W.D. Fairlie, J.M. Matthews, S.M. Valenzuela, M.R. Qiu, W.M. Wu, S. Pankhurst, A.R. Bauskin, S.J. Harrop, et al. 2002. Recombinant CLIC1 (NCC27) assembles in lipid bilayers via a pH-dependent two-state process to form chloride ion channels with identical characteristics to those observed in Chinese hamster ovary cells expressing CLIC1. *J. Biol. Chem.* 277:26003–26011. <https://doi.org/10.1074/jbc.M203666200>
- Wu, X., P.A. Northcott, A. Dubuc, A.J. Dupuy, D.J. Shih, H. Witt, S. Croul, E. Bouffet, D.W. Fults, C.G. Eberhart, et al. 2012. Clonal selection drives genetic divergence of metastatic medulloblastoma. *Nature*. 482: 529–533. <https://doi.org/10.1038/nature10825>
- Zhang, S., X.M. Wang, Z.Y. Yin, W.X. Zhao, J.Y. Zhou, B.X. Zhao, and P.G. Liu. 2013. Chloride intracellular channel 1 is overexpression in hepatic tumor and correlates with a poor prognosis. *APMIS*. 121:1047–1053. <https://doi.org/10.1111/apm.12093>
- Zhang, J., C.M. Carver, F.S. Choveau, and M.S. Shapiro. 2016. Clustering and Functional Coupling of Diverse Ion Channels and Signaling Proteins Revealed by Super-resolution STORM Microscopy in Neurons. *Neuron*. 92:461–478. <https://doi.org/10.1016/j.neuron.2016.09.014>
- Zhu, S., J. Wildonger, S. Barshow, S. Younger, Y. Huang, and T. Lee. 2012. The bHLH repressor Deadpan regulates the self-renewal and specification of Drosophila larval neural stem cells independently of Notch. *PLoS One*. 7: e46724. <https://doi.org/10.1371/journal.pone.0046724>

Supplemental material

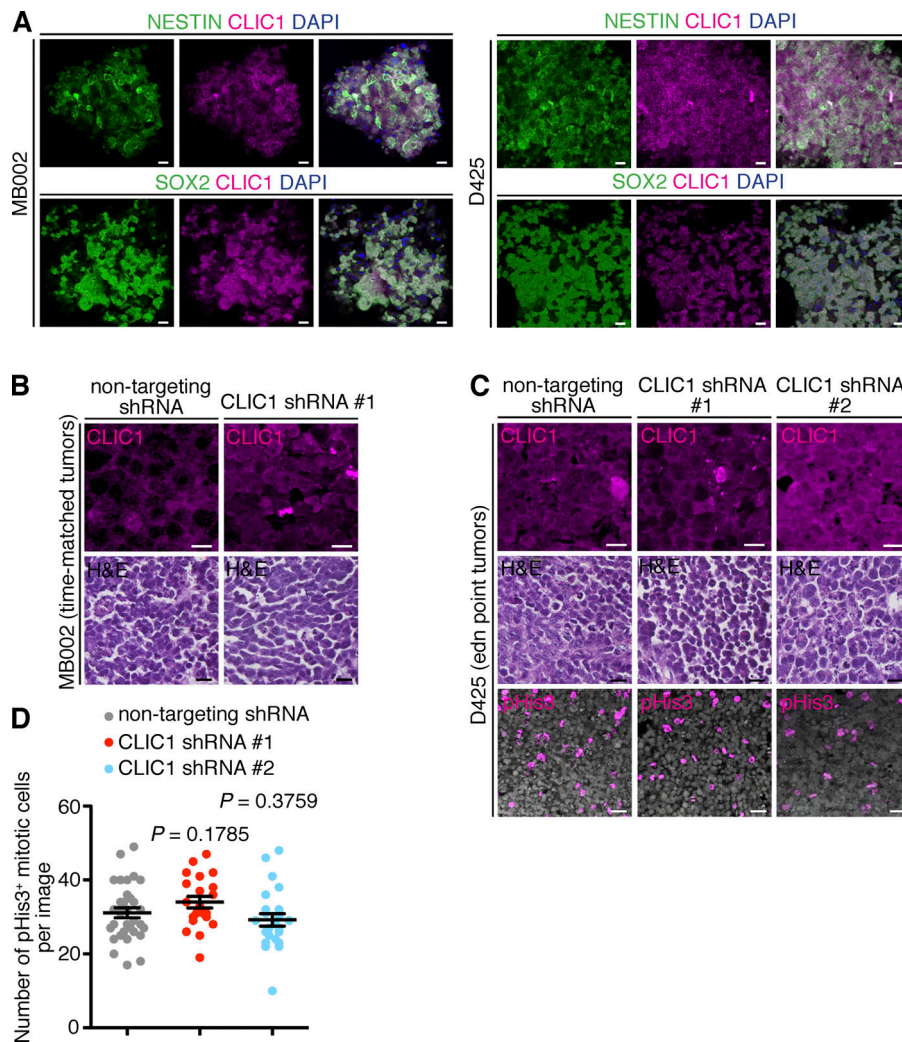


Figure S1. **Characterizations of human MB cell lines and xenograft tumors.** (A) Immunofluorescence staining of MB002 or D425 MB cell spheres show that the cells coexpress CLIC1 and the neural stem cell markers NESTIN and SOX2. Scale bars = 20 μ m. (B) Nontargeting shRNA- and CLIC1 shRNA-treated MB002 xenograft tumors display comparable CLIC1 expression and histology. Scale bars = 30 μ m. (C) Nontargeting shRNA- and CLIC1 shRNA-treated D425 xenograft tumors display comparable CLIC1 expression, histology, and mitosis. Scale bars = 30 μ m. (D) Nontargeting shRNA- and CLIC1 shRNA-treated D425 xenograft tumors display comparable mitotic index. Data represent mean \pm SEM. P values were obtained using unpaired two-tailed Student's t test. For A–D, three biological replications were performed in three independent experiments.

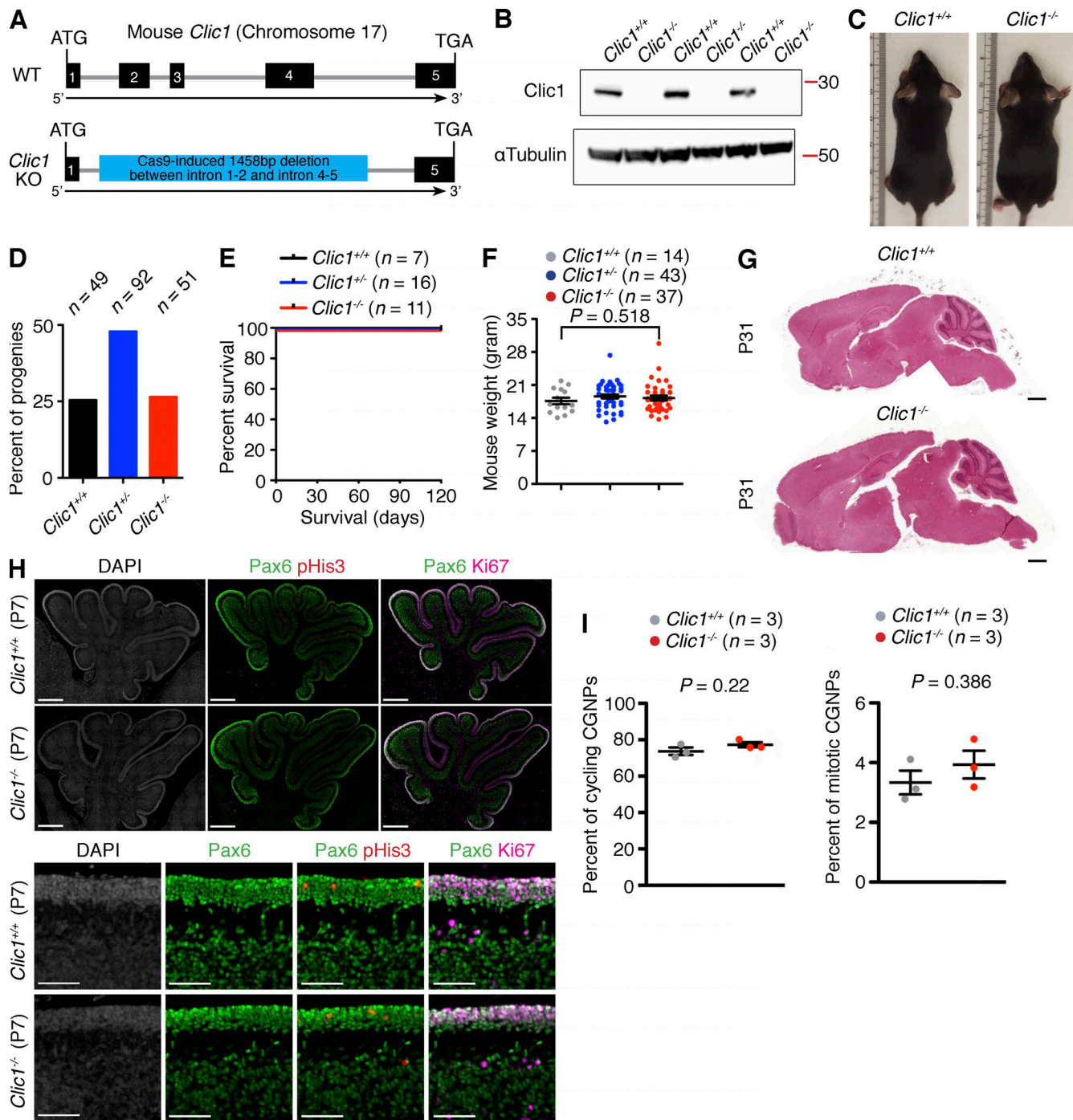


Figure S2. ***Clic1* knockout does not affect mouse development, survival, or body weight.** (A) The CRISPR-Cas9 technique was used to generate a *Clic1* knockout mouse line by deleting 1,458 bp between introns 1 and 5. (B) Western blotting shows the absence of *Clic1* protein in *Clic1*^{-/-} mice. (C) *Clic1*^{+/+} and *Clic1*^{-/-} mice display comparable external morphology at P31. (D) *Clic1*^{+/+}, *Clic1*^{+/-}, and *Clic1*^{-/-} mice are born at Mendelian ratio. (E) *Clic1*^{+/+}, *Clic1*^{+/-}, and *Clic1*^{-/-} mice display comparable survival within the observation timeframe of 120 d. (F) *Clic1*^{+/+}, *Clic1*^{+/-}, and *Clic1*^{-/-} mice display comparable body weight. (G) The brains of P31 *Clic1*^{+/+} and *Clic1*^{-/-} mice display comparable morphology. Scale bars = 1 mm. (H) P7 *Clic1*^{+/+} and *Clic1*^{-/-} mice display comparable cerebellum architecture and proliferation at the external granule neuron layer. Scale bars for top and bottom images represent 300 μm and 50 μm, respectively. (I) CGNPs of P7 *Clic1*^{+/+} and *Clic1*^{-/-} mice display comparable cycling and mitotic capacity (three biological replications, two independent experiments). For B, G, and H, n = 2 independent experiments (three biological replications). For C–F, n = 2 independent experiments (at least five mice per genotype). For F and I, data represent mean ± SEM. P values were obtained using an unpaired two-tailed Student's *t* test.

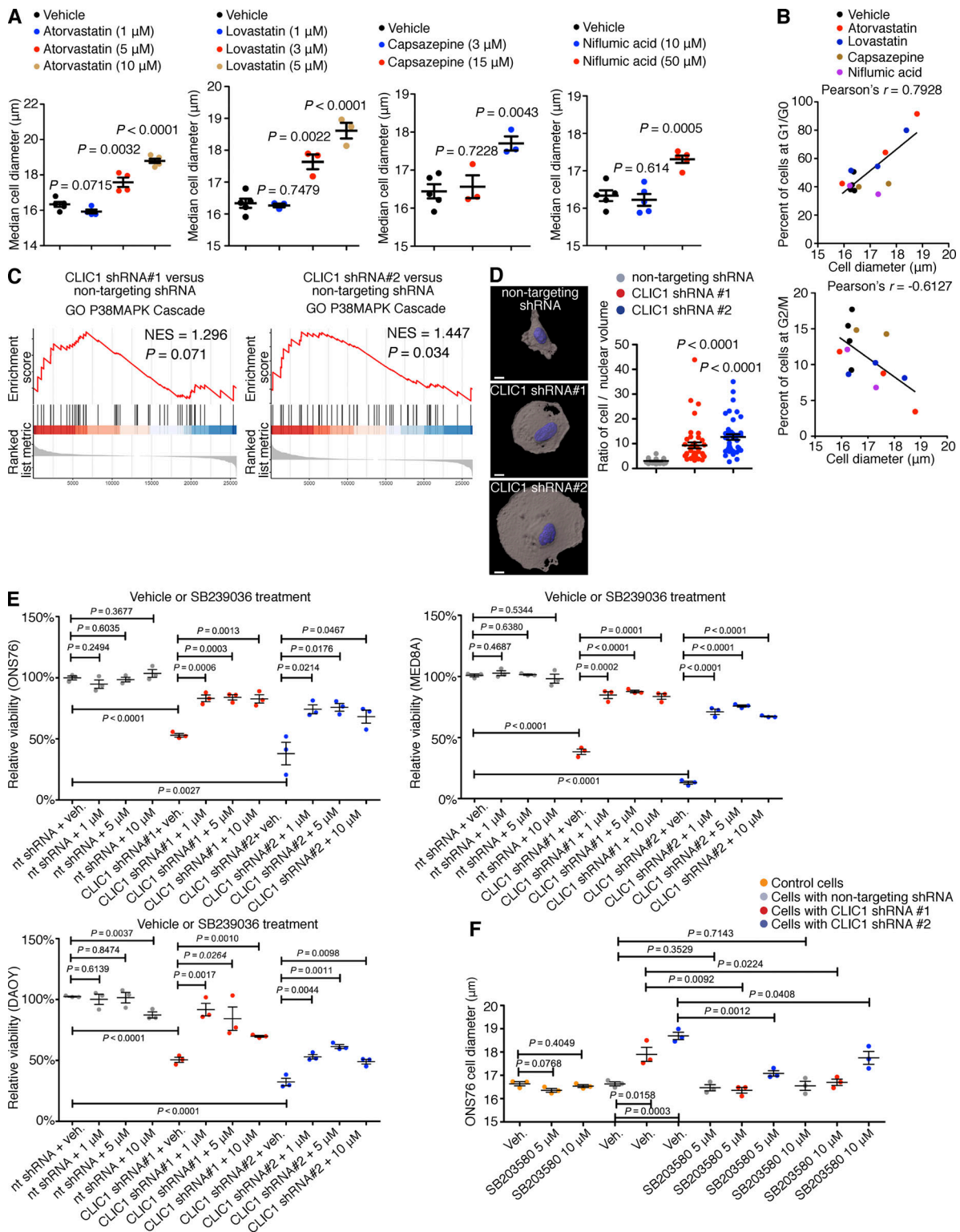


Figure S3. **Cell volume, cell cycle, and p38 MAPK analyses.** (A) Atorvastatin, lovastatin, capsazepine, and niflumic acid treatment results in dose-dependent increase of MB cell diameter. Data represent mean \pm SEM. P values were obtained using unpaired two-tailed Student's *t* test (three to five biological replications, three independent experiments). (B) Pearson's correlation between MB cell volume and cell cycle phases. Pearson's correlation coefficient (*r*) value is indicated on the graphs (three to five biological replications, three independent experiments). (C) CLIC1 knockdown leads to expression of p38 MAPK pathway target genes of ONS76 cells (three biological replications, two independent experiments). GO, Gene Ontology; NES, normalized enrichment score. (D) CLIC1 knockdown increases the cytoplasm/nucleus ratio of ONS76 cells. Scale bars = 10 μ m. (E) p38 inhibitor SB239036 rescues the growth suppression after CLIC1 knockdown in a dose-dependent manner. nt, nontargeting. (F) p38 inhibition partially suppresses the cell volume increase phenotype upon CLIC1 knockdown, while it does not affect cell volume in control or nontargeting shRNA-treated MB cells. For D–F, data represent mean \pm SEM. P values were obtained using an unpaired two-tailed Student's *t* test (three biological replications, three independent experiments).

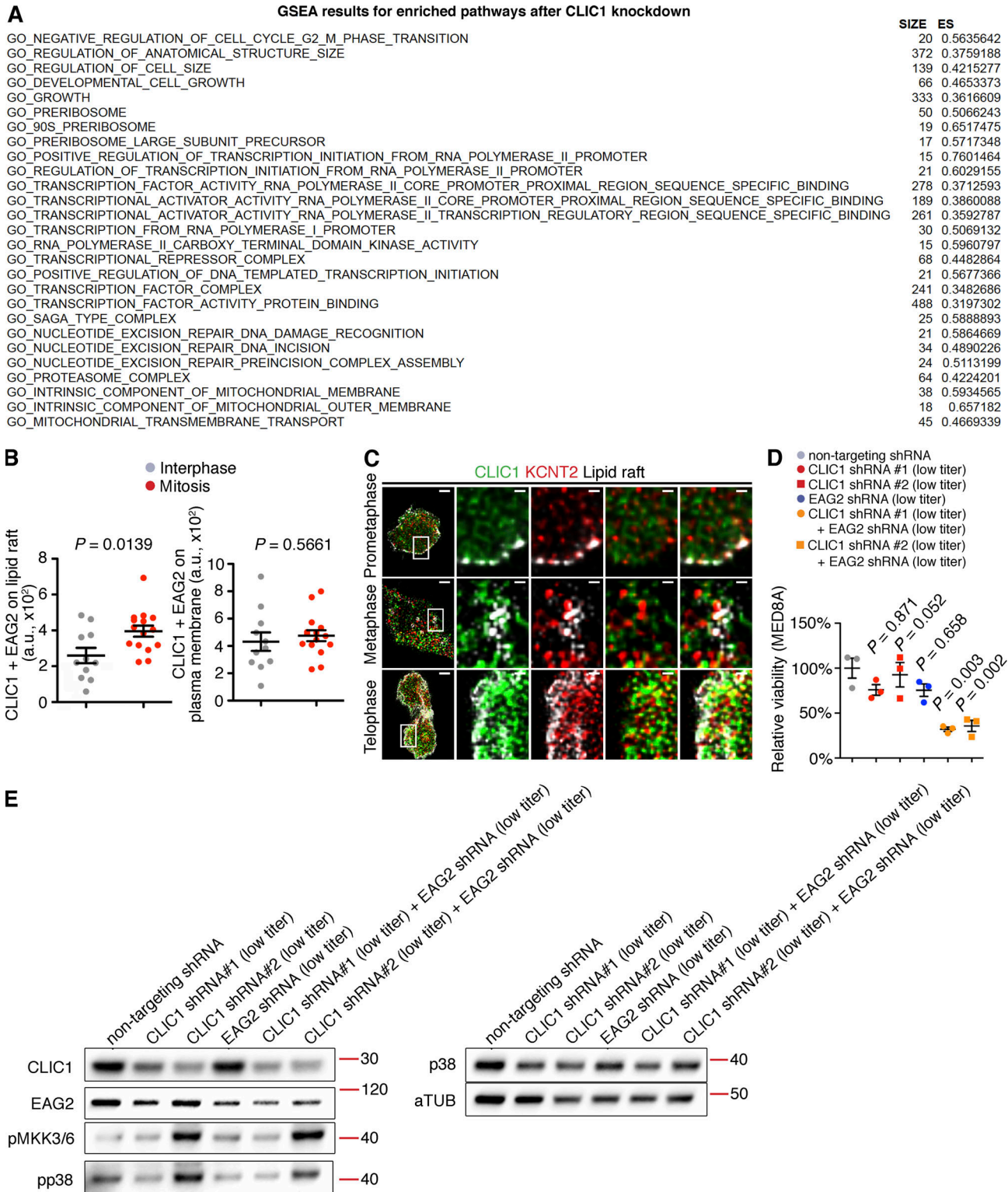


Figure S4. **CLIC1 and KCNT2 localization and identification of CLIC1-correlated ion channels in MB.** (A) Enriched pathways after CLIC1 knockdown in DAQY cells (three biological replications, two independent experiments). (B) CLIC1 and EAG2 display increased colocalization on the lipid rafts during mitosis compared with interphase. Data represent mean \pm SEM. P values were obtained using unpaired two-tailed Student's *t* test (three biological replications, two independent experiments). (C) Immunofluorescence staining shows that CLIC1 and KCNT2 do not display overt colocalization at lipid rafts in the ONS76 cells at various phases of mitosis (three biological replications, two independent experiments). Scale bars for leftmost column images represent 3 μ m and 0.6 μ m for zoomed-in images. (D) Combinatorial RNAi knockdown of CLIC1 and EAG2 display synergistic effect in decreasing the viability of human MB cells (MED8A). Data represent mean \pm SEM. P values were obtained using unpaired two-tailed Student's *t* test (three biological replications, five independent experiments). (E) Western blotting shows increased phosphorylation of MKK3/6 and p38 in ONS76 cells with CLIC1, EAG2, or CLIC1 + EAG2 knockdown compared with the control cells (three biological replications, two independent experiments).

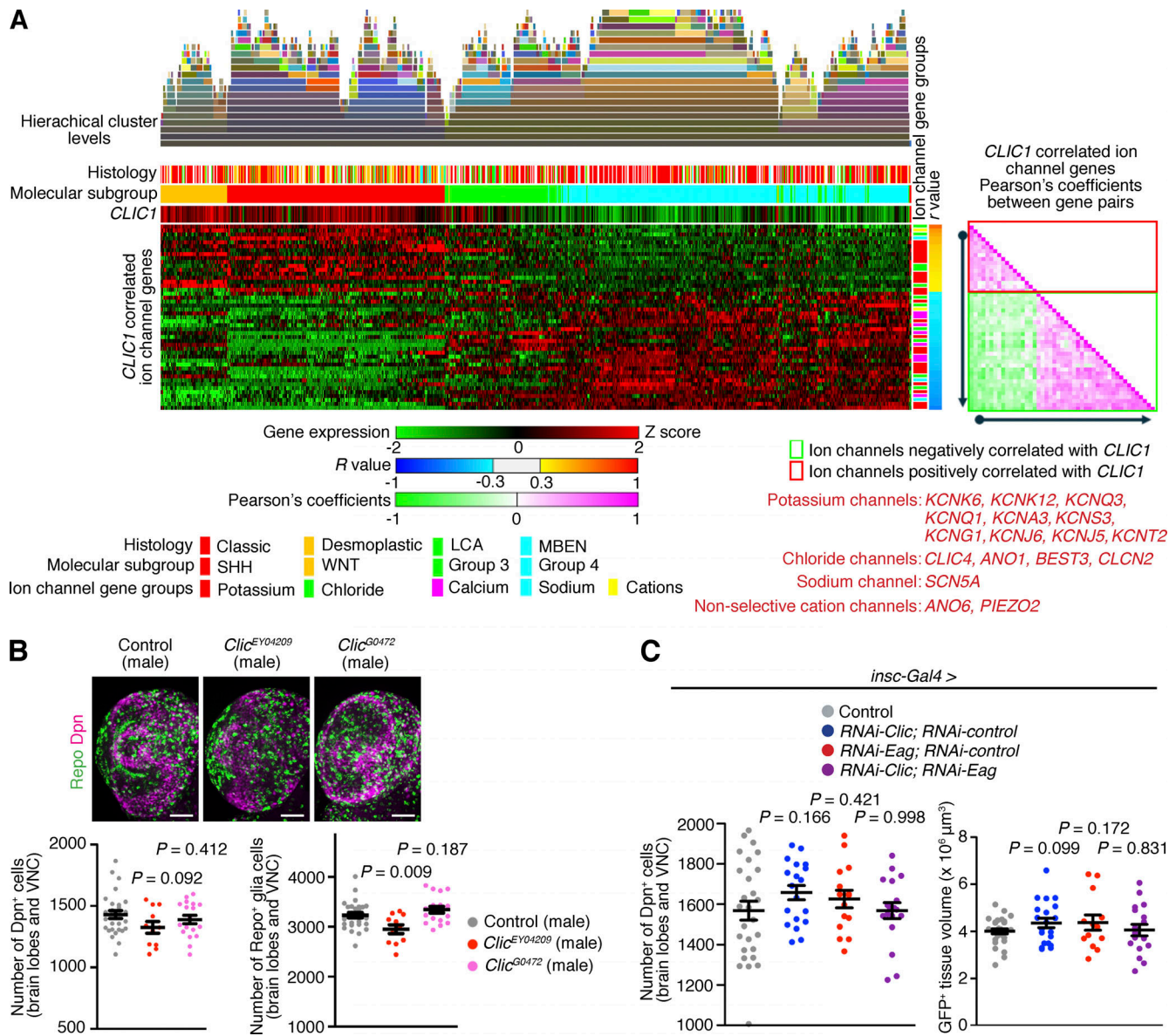


Figure S5. **Clc** mutations and RNAi knockdown of **Clc**, **Eag**, or both **Clc** and **Eag** do not elicit a detectable phenotype in larval neuroblast, progenitor, or glia cells. **(A)** Bioinformatic study of MB gene expression dataset reveals a list of ion channel genes whose expression correlates with the expression of *CLIC1*. Potassium channels, including *KCNT2*, represent the most enriched ion channel genes in the list. Z scores, *R* values, and Pearson's correlation coefficient values are indicated in the heatmaps. **(B)** Representative images and quantifications show that *Clc^{EY04209}* or *Clc^{G0472}* mutation does not significantly alter the number of Dpn⁺ or Repo⁺ cells. Scale bars = 40 μm. **(C)** Either **Clc** or **Eag** knockdown alone, or double ion channel knockdown does not elicit noticeable difference in the number of Dpn⁺ neuroblast and progenitor cells, or the volume of *insc-Gal4*-driven mCD8-GFP-labeled neural tissue. For B and C, data are mean ± SEM. *P* values were obtained using unpaired two-tailed Student's *t* test. 10 to 30 fly larvae brains per genotype were analyzed in three independent experiments.